A machine learning-based perspective on deep convective clouds and their organisation in 3D. Part II: Spatial-temporal patterns of convective organisation

Sarah Brüning[1] and Holger Tost[1]

[1]Institute for Physics of the Atmosphere, Johannes Gutenberg University Mainz, Johann-Joachim-Becher-Weg 21, Mainz, 55128, Rhineland-Palatinate, Germany

Correspondence: Sarah Brüning (sbruenin@uni-mainz.de)

Abstract. This ~~sequence of papers examines~~ series of papers explores spatio-temporal patterns of convective cloud ~~activity~~ occurrence and organisation. ~~In response to the limitations of current remote sensing sensors, our analysis employs a machine learning (ML)-based~~ We use a machine learning-based method to extrapolate a contiguous 3D ~~extrapolation~~ cloud field of 2D satellite data. In Part 2, we ~~investigate spatio-temporal patterns of convective organisation over West Africa and assess their connection to~~ focus on convective organisation in tropical West Africa between March and August 2019, examining how it relates to the 3D ~~convective cloud and core properties. We employ three organisation indices (COP, SCAI,~~ properties of convective clouds and their core structures. We quantify organisation using three indices (SCAI, COP, ROME) to ~~statistically quantify convective organisation. Our results show that convective organisation increases for long-lasting mesoscale cloud systems with numerous deep convective cores. It is likely connected to the Inter-Tropical~~ capture different aspects of spatial cloud clustering. Our analysis emphasises that the most important distinction between all detected clouds and strong convective organisation may relate to a larger cloud area, a lower cloud top and core height, and a shorter lifetime. Weak convective organisation tends to occur with smaller clouds with fewer cores, and a shorter lifetime. We find that convective organisation may occur more frequently in the northern hemisphere during boreal summer months, likely linked to the northward migration of the Intertropical Convergence Zone (ITCZ)~~and its northward shift in summer. In spring (March–May),~~ . From March to May, patches of strong convective organisation ~~appears around the Gulf of Guinea and~~ emerge along the African coastlines and over the remote Atlantic Ocean~~between 15–30° S. The seasonality of convective cloud development induces an increase of the indices between 5–20 % in summer. For instance, the landmass distribution and the influence of extra-tropical dynamics may cause a considerably higher variability in the southern hemisphere. Over the ocean, the organisation indices (COP, SCAI) are about 5–10 % higher than over land~~. Between June and August, hotspots shift inland, particularly across the Sahel and wider West African plains. Notably, oceanic regions show slightly stronger organisation overall. However, ~~derived statistics may be affected by overlapping effects of isolated and clustered convection occurring in the same region. To disentangle their impact calls for an adaptive index. To summarise, combining the information of multiple remote sensing instruments may deliver more profound insights into convective organisation . For future research, we emphasise a further need for a robust quantification of convective organisation~~overlapping regions of strong and weak organisation may complicate the interpretation of regional

statistics. While the machine learning-based 3D perspective helps bridge observational gaps in the representation of cloud structures, the inherent complexity and variability of convective organisation highlight the need for continued investigation.

Copyright statement.

1 Introduction

~~Through its contribution to weather and climate variability, atmospheric~~ Atmospheric convection plays an essential role in the climate system through its contribution to weather and climate variability (Brune et al., 2020). In the tropics, we observe convective clouds forming as spatially connected structures of extensive size (Houze, 1977). These mesoscale convective systems (MCSs) are one of the main drivers for the transport of heat and moisture through the atmosphere. Furthermore, they ~~enhance~~ affect the hydrological and radiative variability ~~(Hartmann et al., 1984). MCSs frequently induce~~ on Earth (Hartmann et al., 1984). The spatial clustering of convective systems - also known as convective organisation - may promote the occurrence of severe weather events such as hail and floods ~~(Jin et al., 2022). Recent changes in the large-scale behaviour of convective clouds, notably the degree of spatial clustering (or convective organisation), emphasise MCSs may promote a future increase in precipitation extremes~~ (Becker et al., 2021). However, ~~results for~~ a robust assessment of the connection between convective organisation and ~~weather extremes are ambiguous. Tan et al. (2015) express~~ extreme weather, in particular in a future climate under global warming, expresses the need for further research~~on how spatial patterns of convection might change under global warming~~.

~~While convective organisation (or aggregation) of deep convection~~ Although the term convective organisation has become increasingly popular in climate research, it is often used vaguely. Mapes and Neale (2011) broadly summarise organisation as "non-randomness in meteorological fields in convecting regions". This definition induces a clustering of deep convective cells which is ubiquitous in the ~~tropics~~atmosphere, particularly in the tropics. However, the underlying mechanisms remain insufficiently understood ~~and may not be well represented in current climate models (Muller and Bony, 2015). An organised state occurs at multiple scales between 100–1000 km and describes how deep convective cells merge into coherent structures such as squall lines, mesoscale convective complexes, or tropical cyclones (Tan et al., 2015; Bläckberg and Singh, 2022). The spatial~~ (Muller and Bony, 2015). While convective organisation is difficult to quantify in observational data, idealised model configured in radiative-convective equilibrium (RCE) could demonstrate a large-scale clustering of convective clouds which is known as self-aggregation of convection (e.g, Held et al. (1993); Wing et al. (2017)). It occurs on a timescale between days and weeks and describes the transition of an approximately random distribution of convective ~~clouds is not arbitrary. Instead, it~~ cells into convecting and non-convecting regions that grow upscale over time. Convective aggregation is driven by either internal dynamics, like cold pools and radiative feedback, or external forces, such as the land-sea-breeze ~~and other large-scale flows~~ (e.g., Haerter et al. (2019), Coppin and Bony (2015), Dauhut et al. (2016)). ~~Furthermore, aggregation~~ Self-aggregation increases with the size and proximity of convective clouds and affects the radiative feedback, large-scale circulation, and

moisture distribution in the vicinity of a cloud cluster (Hartmann et al., 1984). ~~In~~ For instance, an idealised model setup ~~,~~ shows that an aggregated state ~~shows a single region of convective activity surrounded by a drier atmosphere. The~~ consists of a single moist region surrounded by dry regions. Moreover, the feedback between convection, surface fluxes, and radiation further drives aggregation (Tobin et al., 2012). Research shows that self-aggregation may increase with a warming climate (Wing et al., 2020). However, there remain uncertainties connected to a large model spread (Bläckberg and Singh, 2022). ~~Former studies agree that the degree of convective aggregation increases with the size and proximity of contiguous convective regions (Tobin et al., 2012). Therefore, an extensive MCS with several regions of convective activity is often associated with stronger convective organisation than isolated convective cells.~~

~~Overall, convective organisation is complex to define, in particular when using observational data (Brune et al., 2020). There has yet~~ Despite these insights derived from models, identifying and quantifying convective organisation in observational data persists to be a ~~consensus on quantifying the organisational behaviour of convective clouds (Biagioli and Tompkins, 2023)~~ challenge. This may be due a high variability in the quality and quantity of observations. In response, previous studies have developed various metrics ~~to characterise convective organisation and to provide~~ aiming towards a deeper understanding about the underlying physical mechanisms~~(Pscheidt et al., 2019). These~~ . The indices analyse the spatial distribution of the clouds within a defined area to ~~assess the organisational state. They~~ estimate the strength of convective organisation (Pscheidt et al., 2019) . For instance, they help differentiate a regularly distributed, randomly distributed, or organised cloud field by using morphological attributes such as the number of clouds, their nearest-neighbour distances, size, shape, pattern, and timing (Pendergrass, 2020; Retsch et al., 2020). ~~So far, the models show convective organisation increases with a warming climate (Wing and Emanuel, 2014). However, there is a lack of evidence about the relationship between aggregation and precipitation extremes (Bläckberg and Singh, 2022). Unlike simulation data, detecting trends of convective aggregation in observational data remains challenging due to the limited extent and quality of historical records and the large variability and low frequency of events most relevant for aggregation (Pendergrass, 2020). In the future, ensuring~~

Providing timely forecasts and a robust climate risk assessment requires even more a correct representation of convective organisation.

~~Although convective organisation has been the subject of studies using simulation (e.g., Wing et al. (2017); Tompkins and Semie (2017);) or observation data (e.g., Tobin et al. (2012); Tan et al. (2015)), we lack an assessment of convective organisation on a regional level. So far, it has been~~ While satellite observations has shown that organisation within the tropics ~~can be associated~~ may increase overall with extreme precipitation (Semie and Bony, 2020), we have limited knowledge about convective organisation on a regional level. In this study, we aim to provide a deeper understanding of the relationship between cloud properties and convective organisation on ~~a~~ this regional scale, comparable to the work of ~~(Bao et al., 2024)~~Bao et al. (2024). The area of interest (AOI) covers West Africa and the tropical Atlantic Ocean between 30~~°~~° N–30~~° ~~° S and 30~~° ~~° W–30~~° ~~° E and lies within the Inter-Tropical Convergence Zone (ITCZ). Here, the environmental conditions favour the development of ~~large clusters of deep convective storm cells (Takahashi et al., 2023). These cells, such as MCSs, affect local weather and contribute 50–90 % of extreme rainfall over continental West Africa (Klein et al., 2021; Atiah et al., 2023; Fink et al., 2006). At the same time, food security and a high climate risk expose West Africa to multiple threats (Berthou et al., 2019). Changing atmospheric conditions~~

could intensify those hazards. Achieving an advanced understanding of convective organisation is crucial to assess the impact of climate change. In the AOI, we find a deep convective clouds, which are often associated to heavy rain (Takahashi et al., 2023) . A heterogeneous landmass distribution in the northern and southern hemispheres that controls and land-ocean contrasts may affect the development of convection (Brune et al., 2020). Moreover, convective processes differ over land and sea (Zipser et al., 2006). Over the tropical Atlantic Ocean, the a weaker large-scale forcing is weaker. As a result, we observe may induce lower cloud tops and less intense rain rates than over continental Africa (Futyan and Genio, 2007). The rainfall variability between the individual regions of the AOI substantially depends on the moisture availability and thermal gradients (Berthou et al., 2019). Overall, the West African monsoon (WAM) dominates the West African climate. A strong temperature gradient between the warm Sahara and the colder waters of the Gulf of Guinea drives the WAM (Fontaine and Philippon, 2000). Stronger convection generally leads to an increase in heavy rain, a larger detrainment, and a slightly smaller thick anvil emissivity. For instance, Stubenrauch et al. (2023) found a distinct annual cycle of convective organisation connected to seasonal shifts of the convective cloud properties.

In Part 1 of this sequence of papers, we derived contiguous trajectories of convective clouds and their deep convective core (DCC) regions (Brüning and Tost, 2025). We examined the seasonality regions (hereafter: cores) in 15-minute intervals for a six-month period between March to August 2019 (Brüning and Tost, 2025). In this study, we examined cloud and core properties of tropical convection and the life-cycle of clustered and isolated single-core and multi-core convective clouds. In this paper, we aim to complement the findings by including an in-depth analysis of spatio-temporal patterns of convective organisation. We focus on regional and seasonal differences over land and sea Moreover, we aim to investigate the connection between convective organisation and cloud properties within the AOI. In contrast to our former results, we approximate the organisational state not only by the number of DCCs within a cluster (Jones et al., 2024), but we employ organisation indicesto quantify convective organisation For this purpose, we quantify convective organisation at each point in time by employing three organisation indices. The goal is to derive spatial patterns of organisation and compare their spatio-temporal variability (Biagioli and Tompkins, 2023). Our study is based on employs convective cloud trajectories derived from a 4D time series of contiguous 3D radar reflectivities, which we predict from a machine learning (ML)- based -based extrapolation of 2D satellite data (Brüning et al., 2024). This novel We employ an object-based algorithm to detect and track convective clouds in the predicted radar reflectivity field. This perspective allows a simultaneous coverage of the horizontal and vertical cloud development over large and remote regions. The results may provide detailed insights on the connection between convective organisation and 3D cloud properties. For the analysis, we employ an object-based algorithm to detect and track convective clouds in the predicted radar reflectivity field(cloud and core area) and vertical (cloud and core height) properties in the AOI, including remote oceanic regions over the Atlantic Ocean. Our aim is to identify how regional patterns of organisation change between seasons, particularly regarding the connection between convective organisation and the spatio-temporal variability of convective cloud developmentshowcase how convective organisation is distributed in the AOI within the six-month period. Furthermore, we strive to quantify how differences in the cloud and core properties are connected to a weak or strong convective organisation.

We have divided this article into five further sections. In Sect. 2, we describe the ~~data set~~ dataset used in this study. Section 3 presents an overview of metrics employed to quantify convective organisation. Section 4 contains an overview of the results comprising the spatio-temporal variability of organisation indices and cloud ~~microphysical~~ properties. Section 5 ~~discusses~~ relates our key findings to other studies. Moreover, we discuss some limitations we encountered and evaluate the role of the ITCZ and other environmental drivers for the development of ~~large-scale patterns of~~ tropical organisation. Finally, Sect. 6 contains a summary and the main conclusions.

2 Data

~~For this study, we employ contiguous 3D radar reflectivities derived from~~ To quantify convective organisation over tropical West Africa, we use a ML-based ~~extrapolation of 2D satellite data~~ 3D cloud mask build on the 3D cloud reconstruction method described in Brüning et al. (2024) and the convective cloud detection framework by Brüning and Tost (2025). The following section outlines the workflow for producing the 3D radar reflectivity dataset, detecting convective clouds and cores, and extracting cloud properties (Figure 1). ~~In the following section, we provide a brief description of the approach. A more detailed explanation can be found~~

2.1 Satellite data

To identify, track, and analyse convective clouds, we employ a machine learning (ML) algorithm that generates time series of 3D radar reflectivity fields based on 2D satellite observations, as described in Brüning et al. (2024). The input data ~~for the ML framework originate~~ are derived from the Spinning Enhanced Visible and Infrared Imager (SEVIRI) ~~sensor~~ onboard the Meteosat-11 (MSG) satellite (Schmetz et al., 2002). ~~We use eight satellite channels and exclude information within the visiblespectrum to enable predictions at night (Jones et al., 2023). The ML model is a Res-UNet (Ronneberger et al., 2015) which is primarily trained to reconstruct the 2D vertical cross sections of the~~ The AOI is situated near the nadir of SEVIRI, which is positioned above the Equator at 0° longitude. SEVIRI captures multispectral imagery across 12 channels in the visible, near-infrared, and thermal-infrared ranges. Eleven of these channels offer a temporal resolution of 15 minutes and a spatial resolution of 3 km, while one high-resolution visible channel provides 1 km resolution at nadir. From these, we use eight channels to train our ML model (Table 1).

We employ vertical cross-sections of radar reflectivity from the 94-GHz Cloud Profiling Radar (CPR) onboard the ~~CloudSat~~ polar-orbiting ~~satellite (Stephens et al., 2008). We apply a spatio-temporal matching algorithm to the MSG SEVIRI channels and the CPR cross sections to extract training samples for our model. The output of the~~ CloudSat satellite to validate our ML-based predictions. The CPR is an active radar instrument, which transmits microwave pulses toward Earth to detect vertical profiles of cloud hydrometeors. It has a vertical resolution of 240 m (distributed across 125 bins) and a horizontal resolution of 1.4 km across-track and 1.8 km along-track (Stephens et al., 2008). Our study employs data from the level-2 2B-GEOPROF product. While the CPR has a reduced sensor sensitivity at high altitudes, thin ice clouds like cirrus may be underrepresented. Moreover, the radar may be affected by signal attenuation at low altitudes caused by the topography (Sassen and Wang, 2008)

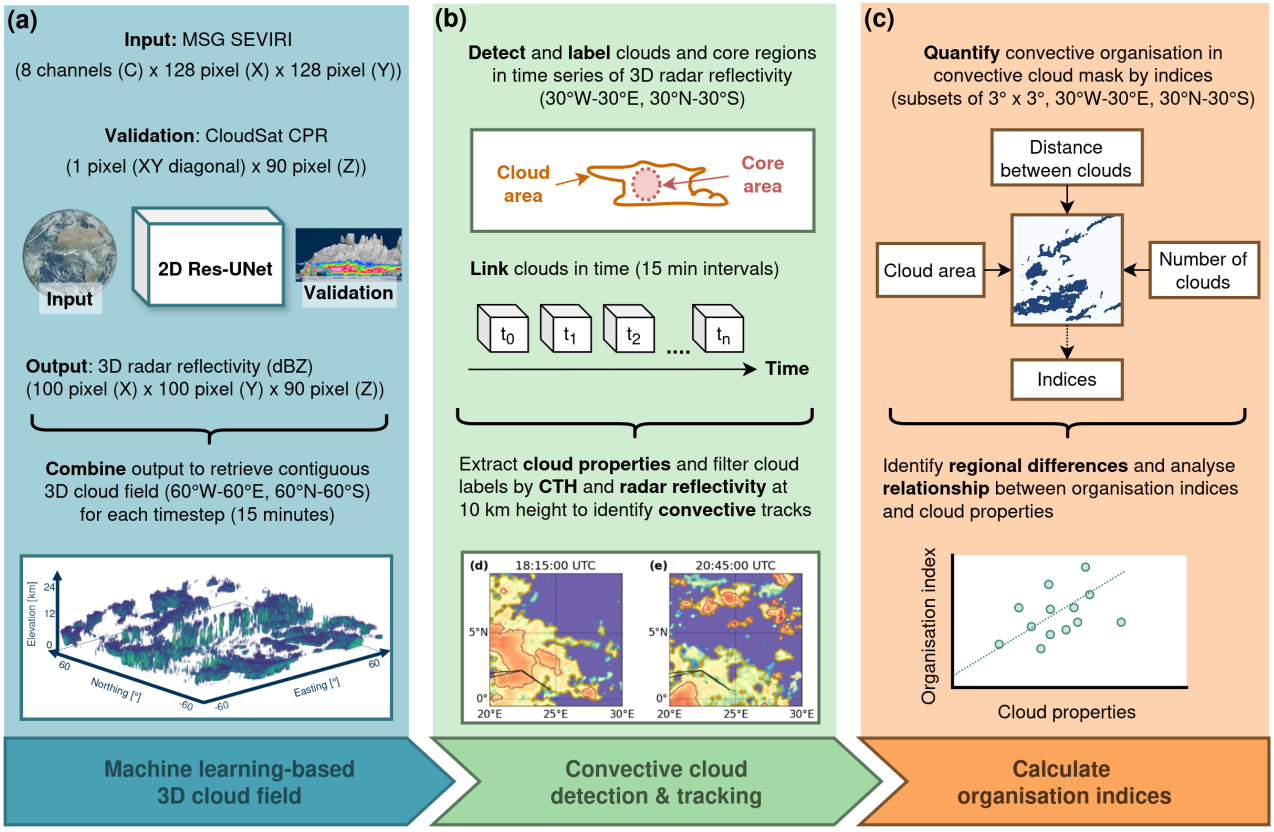

Figure 1. Overview of the workflow for this study. In **(a)**, we show how the derive a contiguous 3D cloud field from 2D data by a machine learning-based extrapolation (Brüning et al., 2024). For this purpose, 2D satellite imagery from the MSG SEVIRI sensor is fed into a 2D Res-UNet and trained to predict a 3D image of radar reflectivities validated against vertical cross sections of the CloudSat CPR. The predictions cover 100 x 100 pixels along 90 vertical bins of 240 m. These patches are combined to cover an area between 60° W–60° E and 60° N–60° S. In **(b)**, an object-based algorithm is employed to detect convective clouds and their cores within the predicted 3D radar reflectivity field. The temporal resolution of the data is 15 minutes. Through each point in time, we link identified cloud objects and filter the trajectories by the cloud top height (CTH), cloud base height (CBH), and number of cores to identify possible convective tracks (Brüning and Tost, 2025). In the current study **(c)**, we aim to quantify convective organisation by calculating organisation indices that are based on the area, distance, and number of objects in each cloud mask. The indices are calculated in 15-minute intervals for a period between March–August 2019. The results are used to analyse regional differences of convective organisation and to describe the relationship between convective organisation and cloud properties.

Table 1. Overview of MSG SEVIRI channels used to predict 3D radar reflectivities in this study.

Channel	Wavelength (μm)	Description	Spatial resolution at nadir	Retrieval at nighttime
IR3.9	3.48–4.36	Near infrared window	3 km	Yes
WV6.2	5.35–7.15	Upper-troposphere water vapour	3 km	Yes
WV7.3	6.85–7.85	Lower-troposphere water vapour	3 km	Yes
IR8.7	8.30–9.10	Mid infrared window	3 km	Yes
IR9.7	9.38–9.94	Ozone sensitivity	3 km	Yes
IR10.8	9.80–11.80	Clean longwave window	3 km	Yes
IR12.0	11.00–13.00	Dirty longwave window	3 km	Yes
IR 13.4	12.40–14.40	CO2 sensitivity	3 km	Yes

. To address these limitations, we limit the data to contain 90 height levels ranging from 2.4 km to 24 km. To improve the ML model performance, we filter the radar reflectivities by the CloudSat cloud mask quality flag to reduce the number of noisy pixels (Marchand et al., 2008).

2.2 3D cloud field reconstruction

In the following section, we describe the methodology used to reconstruct a 3D cloud field, based on the framework developed by Brüning et al. (2024). Our approach utilises a ML algorithm built on the 2D Res-UNet ~~contains not only a reconstruction~~ architecture — a modified convolutional neural network specifically designed for image segmentation tasks (Ronneberger et al., 2015) . The model is primarily trained to reconstruct vertical cross-sections of the CloudSat ~~cross section, but also an extrapolation of the radar reflectivity to a~~ CPR using data from the MSG SEVIRI satellite. Due to the U-Net architecture, the model is capable of producing full 3D radar reflectivity volumes rather than just 2D slices.

The AOI for the reconstructed 3D ~~image, enabling seamless predictions along the whole AOI. We predict the contiguous~~ cloud field spans from 60° W to 60° E and from 60° S to 60° N, corresponding to 2400 × 2400 pixels in the horizontal dimensions. MSG SEVIRI satellite imagery serves as input to the Res-UNet model, setting the horizontal resolution of the 3D ~~cloud tomography for each MSG SEVIRI time step of 15 minutes. Based on the native~~ data to 3 km × 3 km. Initially, we used 11 spectral channels covering the visible, near-infrared, and thermal-infrared ranges. However, the visible channels were excluded in this study to enable daylight-independent predictions (Tables 1 and 2).

The training data consist of 128 × 128 pixel patches of MSG SEVIRI imagery, spatially and temporally aligned with CloudSat overpasses. Each training sample includes a diagonal CPR cross-section. To address the resolution mismatch between MSG SEVIRI and CloudSat, the CPR data are downsampled to match the horizontal resolution of MSG SEVIRI pixels. To mitigate the strong class imbalance between cloudy and cloud-free conditions, cloud-free samples are limited to a maximum of 10 % of the training data. The model is trained on nine months of data and validated on a separate three-month period. It is

Table 2. Modifications applied in this study to the Res-UNet originally proposed in Brüning et al. (2024)

Parameter	Original configuration	Modification
Number of input channels	11	8
Loss function	L2	L1
Nighttime predictions	No	Yes
Average RMSE	3.05	2.99

optimised to reconstruct CloudSat-like 3D reflectivity volumes with a horizontal resolution of 100 × 100 pixels and 90 vertical levels. Predicted radar reflectivity values range from –25 to 20 dBZ and maintain the 15-minute temporal resolution of the MSG SEVIRI ~~images, the data has a spatial resolution of 3 km in the horizontal and 240 m in the vertical dimension.~~ input. An L1 loss function (mean absolute error, MAE) is used during training to evaluate performance. Direct validation is only possible for the diagonal cross-section, which constitutes about 10 % of the data points in each training sample. During the three-month test period, the modified daylight-independent model achieves a root mean square error (RMSE) of 2.99 dBZ, improving upon the original model's average RMSE of 3.05 dBZ (Table 2).

~~The~~ To achieve complete spatial coverage of the domain (60° W to 60° E and 60° S to 60° N), individual 3D output patches are stitched together to form a contiguous volume of 2400 × 2400 × 90 pixels (Figure 1, a). This approach may enable consistent spatial coverage, especially over remote oceanic regions where active sensors are scarce (Prein et al., 2024). Visual inspection confirms that no artifacts are present at tile boundaries, indicating seamless reconstruction across the domain. However, model accuracy tends to decrease with increasing distance from the MSG SEVIRI nadir. Finally, the 3D radar ~~reflectivities are combined into~~ reflectivity volumes are concatenated along the temporal axis to create a 4D ~~time series. Using these data, we~~ cloud field, which is then used to detect and track convective clouds~~and their associated DCCs at each point in time. We define a DCC as a region of high convective activity compared to the cloud anvil. It is characterised by lower temperatures and a strong vertical ascent, which we identify by an extensive vertically contiguous layer and a high radar reflectivity (e.g., Igel et al. (2014); Takahashi et al. (2017)). The workflow for detecting and tracking convective clouds and DCCs follows three steps. At first, we detect convective cloud features by their centroid's position,~~. For the purposes of this study, we crop the domain to 1200 × 1200 pixels, covering the region from 30° W to 30° E and 30° N to 30° S — effectively focusing on the area between the Tropic of Cancer and the Tropic of Capricorn.

2.3 Detection and tracking of convective clouds and cores

Convective clouds are detected and tracked using the *tobac package* (Sokolowsky et al., 2024), which supports an object-based analysis of 3D meteorological data. The detection framework - as described in Brüning and Tost (2025) - proceeds in three stages: the cloud detection and tracking, the core detection, and the classification of potentially convective clouds. We use the ML-based predictions of the radar reflectivity as input data for the detection framework. While radar reflectivity does not

directly measure vertical velocity, it may provide information for detecting hydrometeors associated with convective cloud development (Luo et al., 2008). By merging the 3D data fields along the temporal dimension, we receive a 4D time series that is fed into the tracking algorithm to create continuous trajectories with a temporal resolution of 15 minutes.

We identify potential candidates of convective clouds within the 3D cloud field by applying a fixed radar reflectivity threshold of -15 dBZ. ~~Then, we use a~~ This threshold is used to distinguish hydrometeors from background noise in the radar reflectivity data (Marchand et al., 2008). Although moderately restrictive, this threshold is intended to capture the full spatio-temporal evolution of convective clouds throughout their life cycle, thereby supporting the formation of contiguous trajectories (Esmaili et al., 2016). To reduce noise, we first apply a Gaussian filter with a sigma value of 0.5 to smooth the input data. Next, we compute the centroids of potential cloud structures using a weighted center-of-mass approach, where the weight of each point is determined by its reflectivity value above the -15 dBZ threshold. Each identified centroid is assigned a unique identifier, which is retained throughout the subsequent tracking and segmentation processes. We then apply a 3D watershed segmentation algorithm to delineate the ~~associated cloud field for each centroidand split elongated clouds (Sokolowsky et al., 2024). We assign each identified object~~ volume of individual cloud structures associated with each centroid. The algorithm places markers at the detected centroids within a binary 3D volume, where all other grid points are set to zero. From these markers, the algorithm expands outward through the volume, assigning reflectivity-based pixels to the corresponding cloud until the –15 dBZ threshold is reached. This process produces a labeled 3D cloud mask. Subsequently, we analyse the morphology of each cloud to determine whether any structures might represent a merger of multiple cloud systems. Each cloud's shape is characterised using the best-fitting ellipse, and we compute the aspect ratio — that is, the ratio of the major to the minor axis length. If the major axis is more than 75 % longer than the minor axis, we split the identified cloud into separate objects for further analysis. We track the labeled 3D cloud objects over time by linking them based on their estimated movement speed. At each 15-minute interval, we predict the expected position of a cloud object using its velocity from previous time steps. To streamline this linking process, we define a maximum search radius between time steps, within which only cloud objects are considered potential matches. When new clouds form, we assign them the average velocity of nearby clouds to estimate their likely movement (Heikenfeld et al., 2019). We require a minimum area overlap of 50 % to determine similarity between clouds across consecutive 15-minute intervals.

We aim to detect convective cores for each cloud object at every time step throughout its life cycle. For this purpose, we use the previously generated labeled 3D cloud mask. Core centroids are identified by locating local maxima in a combined metric that incorporates both smoothed radar reflectivity and the vertical extent of a contiguous potential core layer. Specifically, we calculate the mean radar reflectivity for each vertical cloud column, and determine the height of the core layer by counting the number of pixels with reflectivity values greater than 0 dBZ located above 5 km altitude. To fill isolated gaps in otherwise vertically continuous cores, we expand the threshold from 0 dBZ to -5 dBZ in columns that contain at least one pixel exceeding 0 dBZ (Luo et al., 2008; Igel et al., 2014). We then combine both indicators —average reflectivity and potential core vertical depth — for each pixel associated with a cloud label, resulting in a ~~unique label to link their movements through time . Then, we apply a second detection framework for each time step to identify DCCs. Our study employs the ML-based radar reflectivity to approximate the convective updraft (Igel et al., 2014). To detect DCCs, we identify a combined local maxima of the radar~~

Table 3. Cloud and core properties derived from the contiguous convective cloud trajectories.

Feature type	Feature name	Definition
Cloud	Cloud area	Area of the cloud (km^2)
	Cloud top height (CTH)	Height of the cloud (km)
	Lifetime	Lifetime of the cloud trajectory (h)
	Surface type	Value of land-sea mask
Core	Number of cores	Number of identified convective core regions
	Core area	Average area of convective cores (km^2)
	Core height	Depth of the core in the vertical column (km)

~~reflectivity and cloud vertical depth in the~~ 2D layer where we search for local maxima. If at least one local maximum is detected, the corresponding locations are considered candidate core centroids. If no local maxima are found — for example, if no columns contain pixels above 0 dBZ at altitudes higher than 5 km — the cloud is recorded as having zero cores for that time step. Otherwise, we use a 3D ~~cloud field (Feng et al., 2022). Here, the cloud vertical depth describes the difference between the cloud~~ watershed segmentation algorithm to delineate the core volumes surrounding each centroid, allowing for multiple cores to exist within a single cloud at the same time.

2.4 Extraction of cloud properties

We use the labelled cloud masks to extract cloud and core properties at each point in time. Moreover, we compute average properties across the cloud's lifetime to derive distinct key properties that may characterise the trajectory. These properties include the cloud lifetime, cloud area, cloud top height (CTH)~~and cloud base height (CBH)for a vertically contiguous cloud layer (Takahashi et al., 2017). We classify a trajectory as convective when we find at least one DCC, a minimum CTH of 10 km, a maximum CBH of 5 km, and a minimum~~ , number of cores, and mean core area and height (Table 3). The cloud area is computed from the column-wise maximum horizontal extent of the 3D cloud mask, while CTH is derived from the vertical extent. For the cloud lifetime, we extract the time (in hours) between the first and last detection of each trajectory of the labelled pixels. Surface type is assigned via a binary land-sea mask and the modal value for the locations of the cloud trajectory within this land-sea mask. For clouds with one or more cores, we count the maximum number of cores associated to the trajectory. Moreover, the core area and height are derived from the column-wise maximum horizontal extent and vertical extent of the previously identified cores, similar to the cloud area and CTH.

2.5 Filter convective cloud trajectories

We filter the cloud trajectories to exclude possibly non-convective tracks from the analysis. For that purpose, we employ three criteria: (a) One or more core regions for at least 15 minutes, (b) radar reflectivity of higher than 0 dBZ at 10 km height ~~at least~~

~~for~~ for at least 15 minutes, (c) minimum CTH of 10 km and maximum CBH of less than 5 km for at least 15 minutes~~within the cloud (Chen et al., 2021). A more detailed description of the analysis framework is found in the accompanying paper (Brüning and Tost, 2025).~~

~~The AOI is located close to the nadir position of MSG SEVIRI at 0° longitude. Our analysiscomprises 6 months of data from March to August 2019, reflecting the northward shift of the ITCZ in West Africa and the onset of the WAM (Kniffka et al., 2019). The detection framework identifies~~ . While we do not require the convective clouds to have a CTH higher than 10 km at every time step during their trajectory, we discard trajectories that never reach the CTH threshold. After filtering the dataset, we receive 375,~~000 trajectoriesfor the period. After filtering the data to exclude clouds~~ 000 uniquely labeled 3D cloud objects, each associated with a continuous time trajectory and structural information about cloud and core properties (Figure 1, b).

For further analysis, we exclude cloud tracks detected for a single time step of 15 minutes. This results in a refined dataset of 354,073 convective cloud trajectories between March and August 2019. In Fig. 2, we showcase the spatio-temporal distribution of the cloud trajectories. Most clouds are located between 5° S and 20° N, with peak activity from 5°–10° N (Figure 2, a). Approximately 75 % of cloud tracks occur over ocean, with ~~a lifetime of < 1 h, we obtain 300, 000 trajectories for analysing the seasonality of convective organisation between spring (March–May, MAM)and summer (~~land-based tracks comprising the remaining 25 % (Figure 2, b). Most trajectories contain a single convective core (70 %), while the proportion of multi-core systems declines with increasing core count (Figure 2, c). Cloud frequency is higher in March–May (MAM) than in June–August ~~, JJA) .~~ (JJA) (Figure 2, d). The diurnal variability is less pronounced than these monthly differences along the period (Figure 2, e). We observe a high proportion of clouds have a lifetime between 0–3 h (42 %) or 3–6 h (37 %). Hence, about 80 % of the cloud tracks last for less than 6 h. The proportion of cloud tracks with a longer lifetime is considerably lower (Figure 2, f).

While this framework enables a seamless tracking of convective systems along the ML-based 4D time series, it remains subject to several limitations. The predicted data display a ML-based extrapolation of the received CloudSat CPR reflectivities. Hence, they include uncertainties connected to the ML model, such as the blurriness of predictions induced by the loss function which optimizes towards the mean. We receive few information on thin ice clouds due to a reduced sensitivity of the CloudSat CPR to ice clouds in high altitudes (Sassen and Wang, 2008). Moreover, the detection framework rests on an object-based perspective to investigate atmospheric processes. We note the identified trajectories may underlie simplifications caused by an inherent subjectivity of the thresholds applied in the cloud detection step. Nevertheless, the approach may help to bring further insights into the structure and organisation of convective clouds.

3 Method

3.1 Quantifying convective organisation

Convective organisation describes the contrast between convective cells randomly distributed in space and time from those clustering together ~~in an organised state~~ inducing a stronger convective organisation (Pendergrass, 2020). While there exist

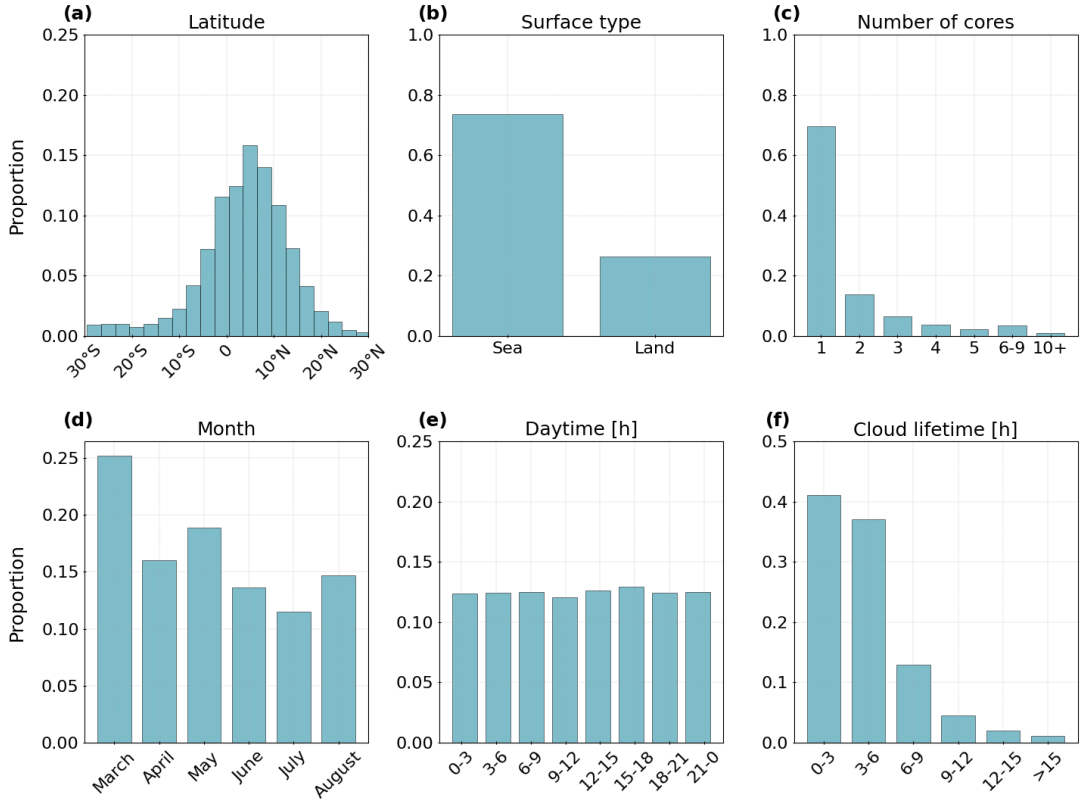

Figure 2. ~~Overview~~ Summary of cloud tracks retrieved between March–August 2019 (n = 354,073). We show the ~~workflow to investigate convective organisation using observational~~ spatial and temporal distribution of the data ~~. The study employs 4D radar reflectivities originating~~ based on **(a)** the latitude grouped in 3° intervals between 30° S and 30° N, **(b)** the surface type derived from a ~~ML-based extrapolation~~ land-sea mask, **(c)** the number of ~~2D satellite data. In Part 1 of this sequence of papers~~cores, ~~we detect convective clouds within~~ **(d)** the ~~predicted radar reflectivities~~ month, **(e)** the daytime, and ~~link them through time to create continuous~~ **(f)** the cloud ~~trajectories~~lifetime.~~In Part 2, these trajectories are used to quantify convective organisation by calculating organisation indices.~~

various organisation indices to quantify the ~~degree of clustering(Biagioli and Tompkins, 2023)~~spatial clustering, each index alone ~~cannot~~ may not sufficiently characterise convective organisation (Stubenrauch et al., 2023). Instead, all indices have specific limitations, such as a sensitivity to the mean cloud area or to the number of individual objects. In response, we chose a combination of three organisation indices ~~(Mandorli and Stubenrauch, 2024). The input for all indices~~ (SCAI, COP, ROME). All indices are designed to work on 2D data. Their input is a binary field, in this case the cloud mask derived in Sect. 2.3, representing the location of ~~labelled~~ labeled convective objects (Semie and Bony, 2020). ~~These cloud labels originate from the convective trajectories described in Sect. 2.~~ We calculate the three organisation indices for the AOI between 30°W–30°E and 30°N–30°S at each timestep of 15 minutes (Figure 1, c).

The first index is the simple-to-compute and straightforward Simple Convective Aggregation Index (SCAI). SCAI describes the ratio of the degree of convective disaggregation to a potential maximal disaggregation within a domain (Tobin et al., 2012). The index is unitless and inversely proportional to the number of grid boxes. SCAI compares the number of objects in the domain (N) and the geometric mean distance (D_0) between the centroid positions of all possible object pairs to the possible maximum number of objects that can exist in the domain (N_{max}) and the characteristic domain size (L).

$$\mathrm{SCAI} = \frac{N D_0}{N_{max} L} 1000. \tag{1}$$

SCAI is a unitless index between 0 and infinity whereas lower values point towards a stronger convective organisation. By design, calculating SCAI requires the presence of multiple cloud clusters~~(Semie and Bony, 2020). It is insensitive to the size of the objects and mainly dominated by the variability in N (White et al., 2018). However, it is less affected by shifts in time and space compared to other indices (Mandorli and Stubenrauch, 2024).~~ .

The Convective ~~Organization~~ organisation Potential (COP) was developed by White et al. (2018) ~~to overcome some limitations of SCAI~~as an adaptation of the I_{org} index. It assumes objects that are larger and closer together are more likely to interact with each other. In contrast to SCAI, the index takes the cloud size into account. COP uses the number of objects (N), the area of the i-th object (A_i) and the j-th object (A_j), and the distance between the centroids of the i-th and the j-th object (d_{ij}). It adds the characteristic domain size (L) and the total image size (L_2). The index is defined by

$$\mathrm{COP} = \frac{2}{N(N-1)} \sum_{i=1}^{N} \sum_{j=i+1}^{N} \frac{\sqrt{A_i/\pi} + \sqrt{A_j/\pi}}{d_{ij}} \tag{2}$$

which is the mean over all the possible pairs of the interaction potential. COP is a positive and unitless index between 0–1 whereas higher values indicate a stronger convective organisation. Larger and closer objects have a higher increase in COP than small and widespread objects (Pscheidt et al., 2019). ~~While the index correctly increases with the proximity and size, it is sensitive to noise caused in a domain with only a few objects (Mandorli and Stubenrauch, 2024).~~

~~SCAI and COP can only be computed when multiple objects are present. In response, we add~~ Additionally, we calculate the Radar Organisation MEtric (ROME)~~to our analysis~~. The index considers the average size, proximity, and size distribution of ~~contiguous convective regions (Retsch et al., 2020)~~convective clouds. Initially, it was designed to analyse radar observations. However, it also worked well with other data (Bläckberg and Singh, 2022). The index assesses connections between pairs of continuous convective regions and assigns a weight to each pair that increases with their respective areas and decreases with

their separation distance. The weight is equal to the area of the larger contiguous convective region plus a contribution from the smaller contiguous convective region that depends on the separation distance (Retsch et al., 2020). It employs the smallest distance between the edges of the i-th and the j-th object in the domain ($\tilde{d}_{ij}$) to define

$$\mathrm{ROME} = \frac{2}{N(N-1)} \sum_{i=1}^{N} \sum_{j=i+1}^{N} \cdot \left[A_{ij}^{(max)} + A_{ij}^{(min)} \cdot min\left(1, \frac{A_{ij}^{(min)}}{\tilde{d}_{ij}^{2}}\right)\right] \quad (3)$$

where $A_{ij}^{(max)} = \max(A_i, A_j)$ and $A_{ij}^{(min)} = \min(A_i, A_j)$. ROME is a positive index measured in units of area. Its value consists of a contribution from the mean area of contiguous convective regions and the distribution of sizes and interaction between different contiguous convective regions. The index is positive, with an increasing ROME value corresponding to a ~~higher degree of aggregation. While ROME is~~ stronger aggregation.

While SCAI and COP are easy to compute, the calculation of ROME is less convenient. Since it has been designed to retrieve information from radar reflectivities, we include the index in our study. In contrast to SCAI and COP, ROME may also be computed when only a single object is present. As evaluated by, e.g., Mandorli and Stubenrauch (2024) and Biagioli and Tompkins (2023), each index has its own strengths and weaknesses. SCAI is insensitive to the size of the objects and mainly dominated by the variability in the number of clouds. However, it is less affected by shifts in time and space which induce high fluctuations of the index values, e.g, due to changes in the resolution of the input image or between two consecutive time steps. In contrast, the calculation of COP includes the object area. While COP correctly increases with the proximity and size, it is sensitive to noise caused in a domain with only a few objects. The index is correlated to the image resolution and shows a high variability for consecutive time steps. While ROME is more noise-safe and independent of the dataset resolution, it strongly connects to the object size~~(Biagioli and Tompkins, 2023).~~

3.2 ~~Grid-based calculation of organisation indices~~

~~Convective organisation occurs on a wide range of scales which are generally larger than 100 km (Bläckberg and Singh, 2022) . We can calculate the indices for a whole domain to assess the overall strength of convective organisation~~. Compared to SCAI and COP, ROME shows a lower variability along consecutive time steps and it is less sensitive to the proximity of objects. Despite these limitations, we employ these indices that have been applied before in our studies to retrieve comparable results. However, ~~investigating regional variability demands a further partitioning of the AOI (Figure 2). For this purpose, we use a grid-based approach and divide the AOI into grid cells with a size of~~ building an adapted methodology for assessing convective organisation may benefit future research.

3.2 Calculating grid-based organisation indices

To assess regional variability in convective organisation, we refrain from computing organisation indices over the entire domain. Instead, the AOI is partitioned into overlapping 3~~° (Semie and Bony, 2020). For instance, further studies applied a varying grid cell size between ~~° × 3° grid cells (e.g., Semie and Bony (2020); Tobin et al. (2012)). Given that the spatial extent and number of convective cloud elements affect the resulting index values, it may be beneficial to mitigate artifacts

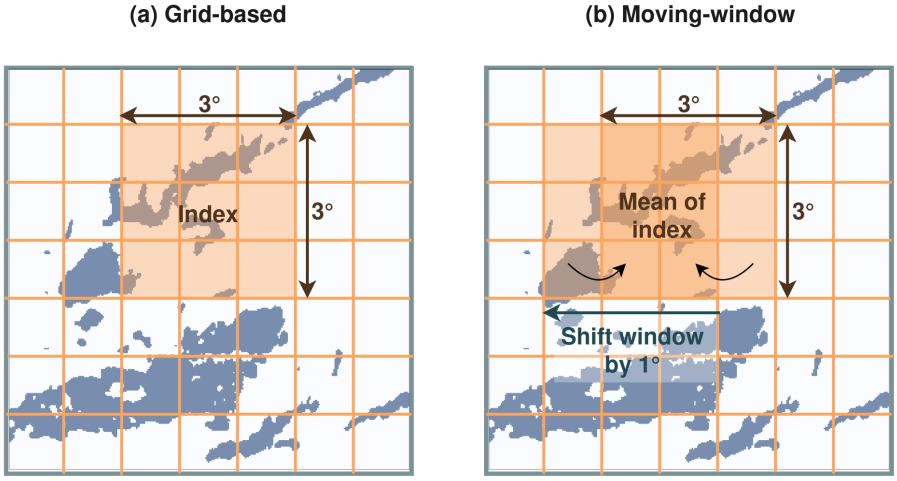

Figure 3. Visualisation of the moving-window approach used to calculate the organisation indices ~~for~~ from the ~~labelled~~ labeled 3D cloud mask. ~~For static~~ When using a fixed grid ~~cells~~ cell size **(a)**, clouds may be split at the ~~grid cell~~ borders leading to an enhanced small-scale value variability between ~~grid cells~~the subsets. In this study, we employ a moving-window which iterates along the grid cells with a kernel size of 1° x 1°. At each iteration, we update the index value by calculating the mean between the index at the former and current subset **(b)**. In contrast to **(a)**, the indices are less influenced by a single grid cell and rather represent the average composed of all window locations.

arising from cloud systems intersecting grid boundaries. In response, we implement a moving-window approach. The initial window is anchored at the northwestern corner of the AOI (27°–30° N, 27°–30° W) and is incrementally shifted by 1° ~~(Jin et al., 2022) and 10° (Tobin et al., 2012) to account for the organisational behaviour of convective clouds. As stated before by Mandorli and Stubenrauch (2024), the number and size of convective clouds highly affect the organisation indices. Choosing an arbitrary grid cell size and location may cut off contiguous clouds, thus affecting the index . That is why we employ a moving window with a kernel size of 1° x 1° to improve the robustness of our results (Jin et al., 2022). Afterwards, we calculate the three~~ ° in both the zonal and meridional directions (Figure 3). For each time step, the spatial organisation indices (SCAI, COP, and ROME) ~~for every time step.~~ are computed within a 3° × 3° window. To enhance statistical robustness and reduce sensitivity to window placement, we calculate a local mean across adjacent overlapping windows, assigning the averaged value to the central grid cell. This approach may reduce boundary-related discontinuities and contribute towards a more stable representation of convective structure, particularly in regions where cloud systems span multiple windows (Jin et al., 2022).

4 Results

4.1 ~~Characteristics~~ Distribution of organisation indices~~in the tropics~~

~~In the following section , we analyse the distribution~~ This section analyses the spatial and temporal distributions of the three ~~organisation indices (COP, SCAI, ROME) to derive spatio-temporal patterns of convective organisation over the AOI.~~

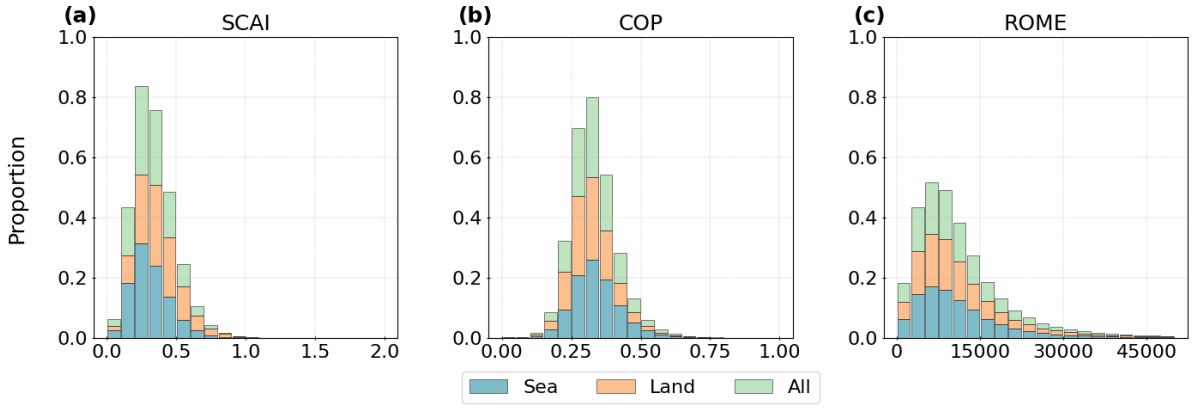

Figure 4. Distribution of convective organisation indices grouped by the surface type. We see the frequencies of **(a)** ~~the~~ COP, **(b)** ~~the~~ SCAI, and **(c)** ~~the~~ ROME~~on a logarithmic scale~~.

~~By design, COP and ROMEbehave anti-proportionally to the values of SCAI (White et al., 2018). However, the frequency distribution shows an overlap of lower index values for all indices (Figure 3) . In Part~~ convective organisation indices: SCAI, COP, and ROME. Lower SCAI values (or higher COP and ROME values) are indicative of enhanced convective clustering, reflecting stronger spatial organisation. Conversely, high SCAI (low COP or ROME) values correspond to more scattered convective structures, implying weaker organisation (Biagioli and Tompkins, 2023).

Figure 4 (a) shows that SCAI values predominantly range between 0 and 1~~of this study (Brüning and Tost, 2025), we found clouds develop about 10 % more frequently over the ocean. This land-sea imbalance is reflected within the frequency distribution of the organisation indices. Most values lie within the lower half of the index scale, either between 0–0~~, with a peak concentration between 0.2–0.4~~for COP and SCAI or between 0–10 000 for ROM. Over land, values are higher in relative terms, in particular for ROME. The results are partly ambiguous as COP and ROME emphasise, on average, a weaker organisation than SCAI~~. Oceanic regions have a slightly higher frequency of SCAI values lower than 0.4, whereas values higher than 0.4 are more common over land. This finding may suggest SCAI detects stronger convective organisation over water. COP values are mainly distributed between 0.1 and 0.75, with the highest density between 0.2–0.45. Over the ocean, values above 0.4 are more frequent, whereas over land, lower values dominate — again pointing to stronger convective organisation over the ocean (Figure 4, b). ROME displays a right-skewed distribution, with most values falling below 15,000. Differences between land and ocean are minor compared to SCAI or COP (Figure 4, c). Overall, the results may indicate a marginally stronger convective organisation over oceanic regions, with ROME showing the weakest land–sea contrast.

~~In Fig. 4, we analyse the distribution of the organisation indices grouped by the surface type. We focus on the diurnal cycle(a–c), zonal changes between~~ Figure 5 compares the diurnal cycle, changes to core numbers, and latitudinal averages of the indices over land and ocean within the 30~~° S and 30° N (d–f), and the relation between each index and the number of DCCs (g–i). Although we observe differences over land and sea, they account for only up to 10 % of the respective index scale~~°

S–30° N domain. For SCAI, we find predominantely lower values over land throughout the day. The diurnal cycle ~~for SCAI is opposed to COP and ROME. All indices indicate the strongest convective organisation in the late evening and early morning hours and the weakest organisation in the afternoon (Figure 4, a–c). The behaviour contradicts the diurnal cycle of cloud formation processes, which show a maximum in the afternoon (land) or late evening (sea) (Cui et al., 2021). In accordance to convective cloud properties, the diurnal differences are lower over the sea than land . The zonal statistics show the weakest convective organisation near the equator and an increase towards the tropics of Cancer and Capricorn (Figure 4, d–f). The highest values of COP and ROME can be found between 10–25° N and S. The value variability is higher~~ exhibits minima between 09:00–12:00 UTC and 21:00–00:00 UTC, particularly over land. SCAI increases between 00:00–06:00 UTC and 12:00–21:00 UTC (Figure 5, a). COP shows a weaker temporal variability than SCAI but with values consistently suggesting higher organisation over the ocean (Figure 5, d). Diurnal variations in SCAI and COP reach up to 10 % of the indices' scales. ROME shows daytime (06:00–18:00 UTC) and nocturnal (00:00–03:00 UTC) peaks over land and mostly nocturnal peaks (21:00–06:00 UTC) over the ocean (Figure 5, g). Collectively, the indices indicate maximum convective organisation occurs over land in the afternoon and over the ocean ~~of the southern hemisphere and land in the northern hemisphere. For SCAI, we observe the lowest values over land between 20–30° N and~~ in the ~~ocean between 15–25° S. All three indices point towards a stronger convective organisation with an increasing number of DCCs (Figure 4, g–h). COP and SCAI show a higher organisation over the ocean, whereas ROME is higher over land~~ night and early morning; minima occur at night over land and from noon to afternoon over the ocean. ~~The indices' calculation may induce this deviation. In contrast to COP, we can compute ROME when only one labelled cloud is present (Retsch et al., 2020). As a result, a domain with one extensive MCS may have a high ROME but no value for~~ SCAI and ROME decrease with increasing numbers of convective cores (Figure 5, b, h). For ROME, organisation decreases up to five cores but increases beyond six, particularly over land (Figure 5, h). COP~~and SCAI (Biagioli and Tompkins, 2023).~~

~~Comparison of the organisation indices behaviour depending on the surface type for **(a)–(c)** the diurnal cycle, **(d)–(f)** the zonal mean, and **(g)–(i)** the number of DCCs for the COP, SCAI, and ROME. Line plots show the mean value with a confidence interval of 95%, black dashed lines refer to the differences over land and sea.~~

4.2 ~~Assessing the relation between cloud properties and convective organisation~~

4.1.1 ~~Patterns of convective cloud development~~

~~In Fig. 5, we compute a spatial density distribution for the number of DCCs associated with a convective cloud and plot the locations in spring (MAM) and summer (JJA). In spring (MAM), we observe the highest proportion of isolated convective cells primarily over the Guinea-Congo rainforest and secondarily over the West African coastline (Figure 5, a). Clouds with 2–9 DCCs have a peak occurrence between coastal West Africa and the Gulf of Guinea, whereas highly clustered systems predominantly develop over the Atlantic Ocean between 15–30° W and parts of the tropical rainforest~~ by contrast, remains largely unaffected by core number as it points out only a slight decrease of convective organisation with increasing core numbers and an increase for clouds with more than six cores (Figure 5, e). This finding suggests for SCAI a stronger

convective organisation for higher core numbers, which opposes the results for COP and ROME. Latitudinally, all indices show stronger organisation near the equator, although the spatial variability differs for the three indices. As SCAI is sensitive to object numbers, a higher frequency of detected clouds near the equator and less clouds near the borders of the AOI may contribute to the variability of the index (Figure 2, Figure 5, c). COP varies less with latitude, whereas we observe slightly higher values between 20° S–20° N (Figure 5, ~~b–c). In summer (JJA), f~~). For ROME, we find the highest variability between latitudinal averages and surface types with peaks over land between 20° S and the ~~ITCZ shifts to its most northward extent (Kniffka et al., 2019). It induces extensive heating in the Sahel, leading to increased land surface temperature anomalies and a higher frequency of deeper convection (Taylor et al., 2022). The hotspot location of isolated convective clouds shifts towards the West African plains and the rainforest north of Congo (Figure 5, d). Custered systems occur more frequently further away from the Atlantic Ocean and up to the Sahel region~~ equator, and over oceanic regions near the equator and between 20°–30° S (Figure 5, ~~e). The most highly clustered clouds are confined to two peak regions over the Atlantic Ocean close to the coast of Liberia and between the Jos Plateau and the Cameroon mountains (Figure 5, f)~~ i). Compared to other regions in the domain, the results show a considerably stronger convective organisation over the southern Atlantic Ocean (30° S) for SCAI and ROME.

~~In a second step, we group the convective clouds by their anvil size to visualise their spatial distribution . We differ three classes for clouds with an anvil smaller than the population's mean size ($\geq$ 1 000 km^2), anvils between the mean and 10 times the mean ($\geq$ 10 000 km^2), and a third, larger, class. Again, the seasonal variations resemble the northward shift of the ITCZ (Figure 5). In spring (MAM), small and medium-sized clouds have a peak occurrence around the equator with a higher spread towards the Gulf of Guinea for medium-sized clouds (Figure 6, a–b). Large clouds show higher seasonal variations. We observe a peak in the southern hemisphere~~

4.2 Spatial patterns and statistical relationships

Figure 6 presents the spatial distribution of the three organisation indices (SCAI, COP, ROME), along with associated cloud and core properties, interpolated onto a 3° × 3° grid and displayed as latitudinal cross-sections. Distinct regional patterns emerge across the AOI, highlighting potential links between convective organisation and cloud structure. Near the equator - particularly over continental Africa ~~(MAM) (Figure 6, c). In summer (JJA), these former peak regions vanish. The development of MCSs may be affected by alterations of the soil moisture-precipitation feedback or the advection of moist air masses through strong wind shear and convective instability (Nicholson, 2018). Due to the influence of the ITCZ, we see two peaks in the northern hemisphere around the Senegal River and Lake Chad (Figure 6, f). The primary occurrence for small and medium-sized clouds shifts from 5° S–10° Nto 5°–20° N (Figure 6, d–e). We generally find highly clustered clouds to be accompanied by a larger cloud anvil size and vice versa (Figure 5,6).~~

~~Spatial distribution of clouds grouped by their anvil area for spring (MAM, upper row) and summer (JJA, lower row). Clouds are grouped as **(a), (d)** small with an anvil area smaller than 1 000 km^2, **(b), (e)** medium with an anvil area between 1 000–10 000 km^2, and **(c), (f)** large with an anvil area larger than 10 000 km^2. The values represent the normalized density for each distribution.~~

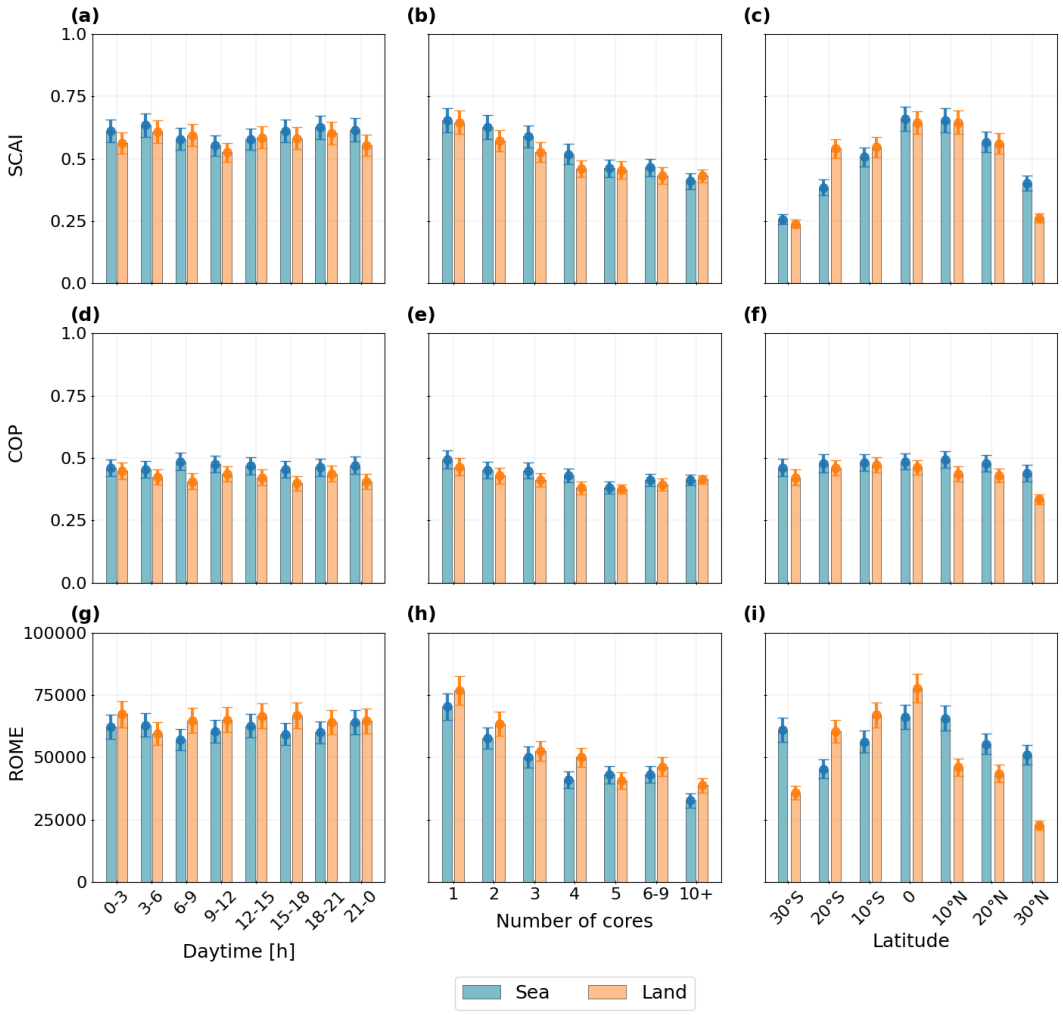

Figure 5. ~~Spatial distribution~~ Comparison of ~~clouds~~ the organisation indices **(a)–(c)** SCAI, **(d)–(f)** COP, and **(g)–(i)** ROME. The columns show the diurnal cycle (grouped ~~by~~ in 3 h intervals), the number of ~~associated~~ cores~~for spring (MAM~~, ~~upper row)~~ and ~~summer~~ the latitude (~~JJA, lower row~~in 10° intervals) ~~. Clouds are~~ grouped ~~as having **(a), (d)** a single core~~by the surface type (land, ~~**(b), (c)** 2–9 cores, and **(c), (f)** 10 and more cores~~sea). ~~The values represent~~ Vertical errorbars show the ~~normalized density for each distribution~~standard error of the mean.

~~The spatial distribution of the cloud and core properties provides information on regional patterns of convective activity in the AOI (Figure 7). Near the equator, we find smaller cloud anvils, higher cloud tops, a reduced cloud lifetime, an enhanced arearatio, -~~ higher SCAI values may coincide with a smaller cloud area, elevated cloud top height (CTH), and ~~slightly fewer and smaller DCCs. These properties are typical for fast-evolving, isolated convective cells, which frequently occur between 15° S–15° N(Feng et al., 2022).~~ taller convective cores. In contrast, ~~clouds with a large anvil come along a lower CTH, higher cloud lifetime, and a higher number of cores. They appear particularly north of 25° N and south of~~ lower SCAI values are found primarily over the Atlantic Ocean and in subtropical zones of northern and southern Africa (15~~° S. We observe extensive patches of large and long-lived convective cells~~ °–30° N/S). These regions are characterized by larger cloud areas, a lower CTH and lower core heights (Figure 6, a, d, e, i). For the cloud lifetime, the number of cores, and the core area, we observe a less distinct connection. They show a high spatial variability along the AOI, whereas a longer cloud lifetime, a higher number of cores, and a larger core area may be related to a smaller cloud area, higher CTH, and higher core height in near-equator regions (< 15° N/S) and to a larger cloud area, lower CTH, and lower core height near the tropics (> 15° N/S) (Figure 6, d–i). COP exhibits low spatial variability, with most values between 0.2–0.5 (Figure 6, b). ROME, in contrast, displays pronounced spatial differences: high values occur between 15°–30° N/S, particularly over the Atlantic Ocean ~~(5–20° S) and the Sahel region (Futyan and Genio, 2007). In the same region, we detect a diverging convective activity regarding the number and size of DCCs. South of 20° S, we find the largest DCCs. However, these convective systems are connected to fewer DCCs, smaller anvils, a lower CTH, and a lower cloud lifetime. In the southern hemisphere, the~~ and near African coastlines, and near the equator over the Gulf of Guinea and continental Africa (Figure 6, c). Over the Sahel, clouds tend to be large, with numerous, wide but relatively shallow cores. Over the South Atlantic (15°–30° S), cloud systems exhibit large areas, long lifetimes, and a high number of cores. This pattern may reflect cloud clustering in the AOI may be influenced by oceanic circulation and adjacent landmasses ~~may contribute to the development of long-lasting clouds in the Atlantic Ocean (Atiah et al., 2023). Our analysis shows a higher variability between the hemisphere and latitude than for the surface type. Moreover, we detect distinct differences between regions closer to the equator and the tropics~~(Atiah et al., 2023). Overall, regions with stronger convective organisation - indicated by low SCAI and high COP or ROME - tend to exhibit smaller clouds with low CTH and core heights. For the number of cores, the core area, and cloud lifetime, a higher regional variability may be apparent. These contrasts are most apparent between equatorial and subtropical regions.

~~We extend the analysis by investigating seasonal differences of cloud and core statistics in spring (MAM)and summer (JJA). Figure 8 emphasises that the seasonality of the convective activity depends on the hemisphere. The cloud~~ To quantify the relationship between organisation indices and cloud properties, we compute Spearman's rank correlation coefficient R using data from all cloud tracks (Figure 7). The logarithmic distributions reveal a general skew toward low values for SCAI, ROME, cloud area, lifetime, number of cores, and core area. The correlation analysis shows that COP and ROME may be positively associated with cloud area~~is larger in spring over northern Africa (> 15° N) and in summer over West Africa and the Atlantic Ocean (< 15° N). We observe an extensive patch of large cloud anvils in the southern hemisphere that grows in summer. At the same time, the cloud anvil areaincreases in regions near the equator. Compared to regions near the tropics, equator-near regions show a lower average and variability in the seasonal cycle (Figure 8, a). The CTH in summer is higher over the Atlantic Ocean~~

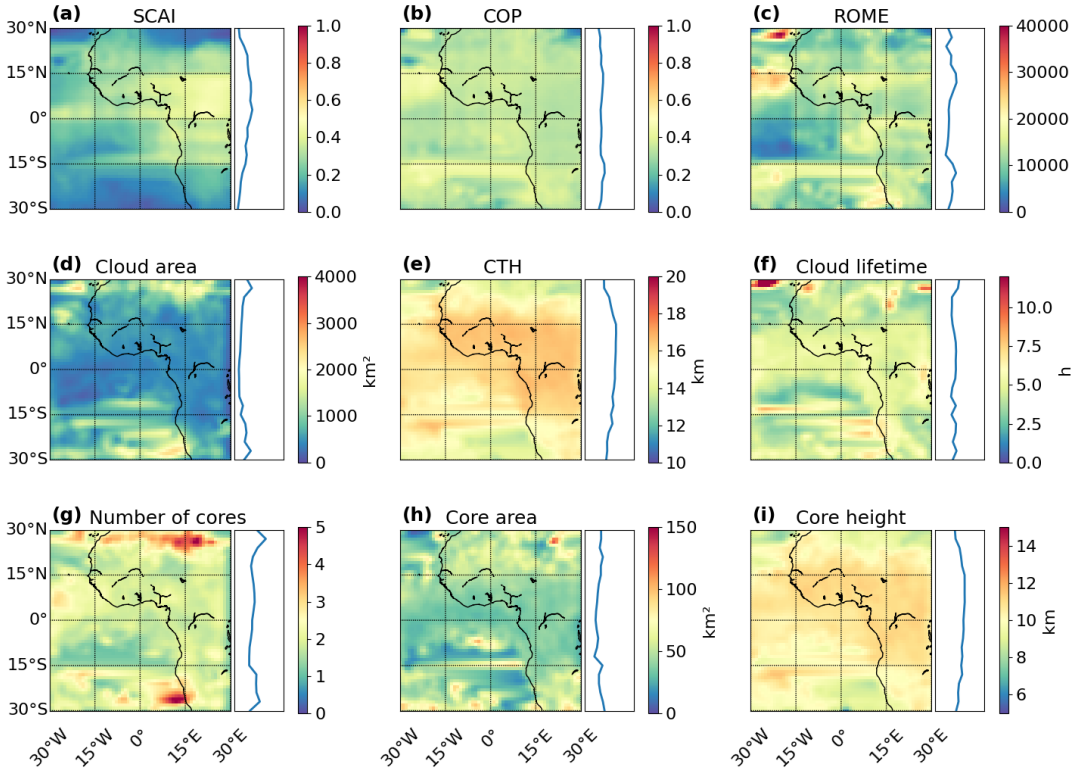

Figure 6. Mean values for ~~cloud and core properties in the AOI interpolated on a 3° x 3° grid. We see~~ **(a)** SCAI, **(b)** COP, **(c)** ROME, **(d)** the cloud ~~anvil~~ area, ~~**(b)**~~ **(e)** the CTH, ~~**(c)**~~ **(f)** the cloud lifetime, ~~**(d)**~~ **(g)** the number of ~~DCCs~~cores, ~~**(e)**~~ **(h)** the convective core size, and **(f)** the ~~area ratio between~~ core height. The plot shows the spatial distribution in the AOI interpolated on a 3° x 3° grid (left) and ~~anvil~~the average for each latitude between 30° N and 30° S (n = 354,073).

~~and the Sahel and lower over coastal West Africa. During this season~~, lifetime, CTH, number of cores, and core height (Figure 7, g–r). In contrast, SCAI is negatively correlated with all of these properties except for CTH and the core height (Figure 7, a–f). For the core area, we see ~~more DCCs, a larger core size, and a reduced area ratio. With some small-scale deviations, convective activity near the equator increases in summer. We find more clustered clouds and intense convection in spring near the tropic of Cancer. In contrast, convective activity near the tropic of Capricorn is higher in summer. Overall, a higher convective activity comes with a lower area ratio, a higher number of DCCs, a larger cloud and core area , and a longer cloud lifetime~~a weak negative correlation to all indices. The findings suggest that stronger convective organisation may be statistically linked to larger, longer-lived cloud systems, a higher CTH and core height, and more cores. Interestingly, these statistical relationships contrast with some spatial patterns in Fig. 6. For instance, while higher ROME values spatially co-occur with smaller clouds and shorter lifetimes in some regions, correlation coefficients suggest that, overall, organisation increases with cloud area and

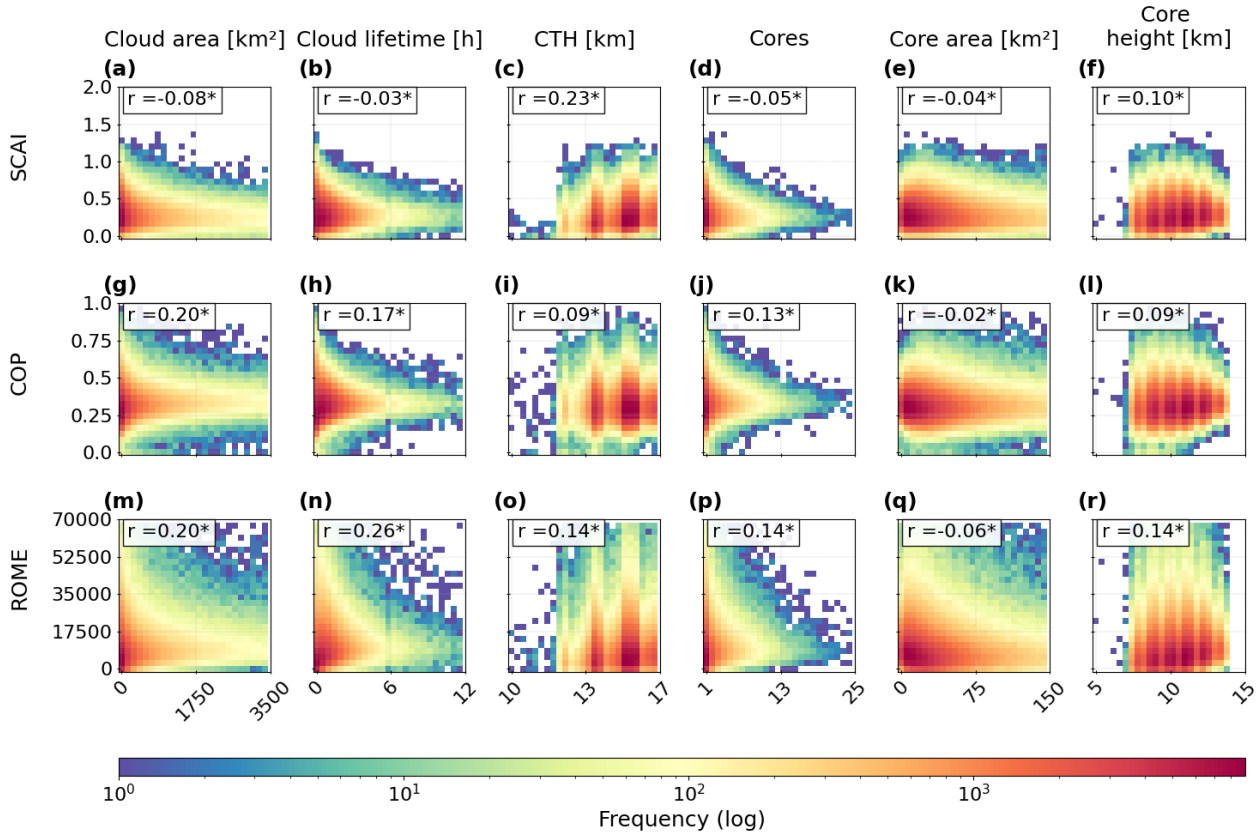

Figure 7. ~~Seasonal differences~~ Histogram showing the logarithmic frequency distribution for ~~cloud statistics in~~ the ~~AOI interpolated on a 3° x 3° grid. We see the difference between spring (MAM)~~ SCAI, COP, and ~~summer (JJA) season for (a)~~ ROME against the **(a, g, m)** the cloud ~~anvil~~ area, ~~(b)~~ **(b, h, n)** the ~~CTH, (c) the~~ cloud lifetime, ~~(d)~~ **(c, i, o)** the CTH, **(d, j, p)** the number of ~~DCC~~scores, ~~(e)~~ **(e, k, q)** the convective core size, and ~~(f)~~ **(f, l, r)** the ~~area ratio between~~ core ~~and anvil~~height. In each histogram, we add the Spearman correlation coefficient R to quantify the strength of the relationship (n = 354,073) (significant with *: p < 0.1).

duration. However, ~~local circulations and the landmass distribution may considerably alter the development of convective cells (Atiah et al., 2023)~~most correlations are weak, with maximum coefficients around 0.26 between ROME and the cloud lifetime. They highlight the complex and regionally variable nature of these relationships.

4.2.1 ~~Identifying regional hotspots of convective organisation~~

4.3 Temporal variability of cloud properties and organisation indices

The previous analysis suggests the overall correlation between convective organisation indices and cloud/core properties is generally weak. In this section, we ~~analyse the spread of the distribution for each organisation index to identify geographical~~

hotspots of convective organisation. For each index, we calculate the 10th (P10aim to capture changes in convective behaviour along the period that may help to explain observed patterns. For this purpose, we filter the dataset into two subsets between March to May (MAM, n = 30 243) and 90th (P90212,984) and June to August (JJA, n = 29 365)percentile as well as the inter-quartile range (IQR) between the 25th and 75th percentile. A hotspot is classified by using the highest (COP, ROME) or lowest (SCAI)141,089). Here, we analyse monthly means over land and ocean (Figure 8). Overall, differences between land and ocean typically span up to 10 % of the data (Semie and Bony, 2020). The IQR of the indices' distribution corresponds to a more random organisation of the clouds.

Section 4.1 shows that the convective organisation is overall weaker around the equator. In this region, we find ahigh proportion of isolated and short-lived clouds (Section **??**). Their impact on large-scale patterns of organisation is limited compared to MCSs (Takahashi et al., 2023). In our study, the locations of clustered clouds (Figure 5)indicate that clouds with multiple regions of convective activity can be found over land and sea, especially during the summer. At that time, the number and size of DCCs increases, in particular around the equator (Section **??**each index's dynamic range (Figure 4). For the monthly changes, most variables do not exhibit a linear trend. SCAI, COP, and the number of cores remain relatively stable, while the CTH and core height vary non-monotonically (Figure 8, a, b, e, g, i). SCAI generally decreases over the ocean and increases slightly over land until June, returning to near-March values by August (Figure 8, a). COP displays similar changes over land, while over the ocean, it increases marginally throughout the period (Figure 8, b). ROME exhibits the strongest variability, increasing over both surface types, especially over the ocean (Figure 8, c). Notably, average CTH, cloud lifetime, and core height are consistently higher over land, whereas cloud and core areas are larger over the ocean, particularly from May to August (Figure 8, d–f, h–i). The percentiles of the organisation indices correspond predominately to locations around the equator and over the Atlantic Ocean in the southern hemisphere. Around the tropics, we find extensive MCSs and high values for COP and ROME. However, the percentiles show that these locations are considerably affected by outliers. The location of the IQR comprises a band spanning between 10° N–10° Snumber of cores remains fairly constant across the time series (Figure 8, g). Over the ocean, we observe a steady increase in cloud and core area and a decrease in CTH. Core height peaks in May and July, followed by a decline in August. Over land, temporal changes are less pronounced, though the core area shows a slight dip until May and then rises again by August.

Figure 9 presents the spatial and latitudinal differences between spring (MAM) and summer (JJA), interpolated on a 3° × 3° grid. Although SCAI exhibits minor variability in average monthly changes (Figure 8, a), its spatial distribution shows a marked increase between 15°–30° N and a decrease south of 15° N — especially across the Gulf of Guinea and central Africa (0°–15° S) (Figure 9, 10). Within that region, we find more randomly distributed convective cells. The band covers the Atlantic Ocean up to the coastal regions between the Senegal and Ivory Coast a). COP remains relatively stable across latitudes north of 15° S, with notable summer decreases south of 15° S, over the Sahel, and near the Canary Islands (Figure 9, b). ROME displays more complex behavior along the period, with an overall increase around the AOI in JJA. We see decreases over northern Africa, the Canaries, and regions south of 20° S, but increases between 15° N and 15° S, particularly near the equator and around 15° S (Figure 9, a-b,g-h,i-j). In spring (MAM), this area reaches up to the Congo rainforest at around 12° S , whereas it shifts northward in summer(JJA) (Figure 7). The least organised clouds (P10 COP/ROME, P90 SCAI)appear c). Seasonal spatial

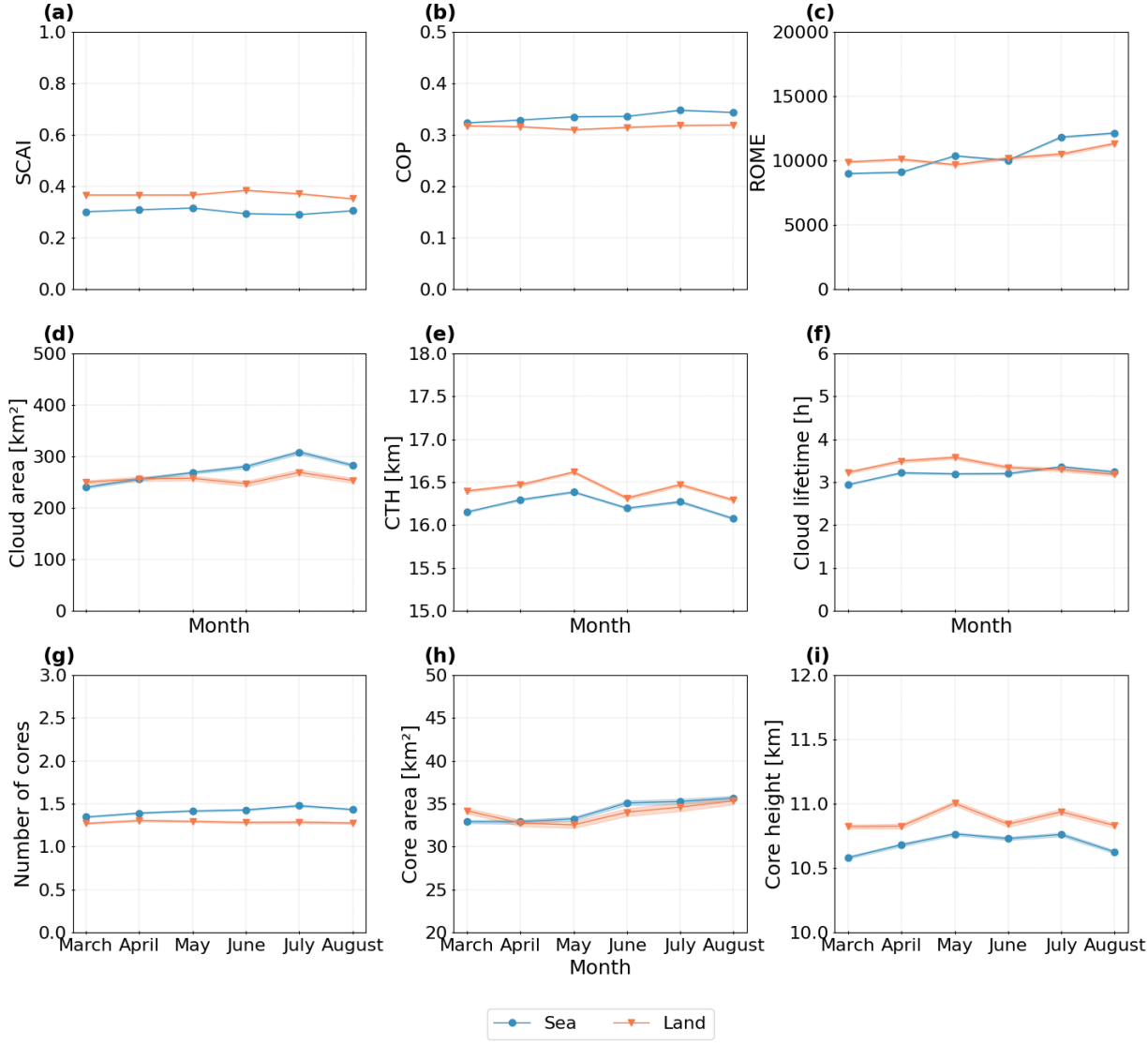

Figure 8. Monthly changes of the organisation indices and cloud and core properties between March and August 2019. We show **(a)** the SCAI, **(b)** the COP, **(c)** the ROME, **(d)** the cloud area, **(e)** the CTH, **(f)** the cloud lifetime, **(g)** the number of cores, **(h)** the convective core size, and **(f)** the core height grouped by the surface type. Line plots show the mean value (solid line) with a confidence interval of 95 %.

patterns of cloud properties mirror those of ROME to some extent. Cloud area and lifetime increase near the equator and at 15° S in summer, but are larger in northern Africa during spring (Figure 9, d, f). CTH shows an opposing pattern, with summer increases north of 15° N and decreases elsewhere, especially south of 15° S (Figure 9, e). The number of cores increases over the Atlantic~~Ocean (5° S–5° N) and the rainforest (~~, West African coastlines, and equatorial rainforests in summer but declines in coastal regions north of 15~~°–30° E). In contrast, most organised clouds (P90 COP/ROME, P10 SCAI)occur around the Gulf of Guinea, coastal West Africa and the Atlantic Ocean (>~~ ° N and south of the equator (Figure 9, g). Core area displays high spatial variability with generally higher summer values, though the pattern is fragmented (Figure 9, h). Core height changes are similar to CTH — rising north of 15~~° S)~~ ° N and decreasing south of 15° S - while equatorial changes are modest and differ by surface type (Figure 9~~),~~ i). Notably, regions south of 15° S show an increase in core area concurrent with reductions in core height and number, potentially reflecting shifts in convective mode. These spatial and temporal differences may reflect the influence of local circulations and land-sea contrasts on convective development, contributing to the observed spatio-temporal heterogeneity across the AOI. ~~In summer, we see a maximum around the Cameroon mountains and the coastal regions around Senegal up to the Nigerian Planes (Figure 10).~~

~~Spatial distribution of convective organisation indices between June and August (JJA) for the COP, SCAI, and ROME. Data points are interpolated on a 3° x 3° grid. Clouds are grouped as strong or weak organised using the **(a,d,g)** 10th (P10), **(b,e,h)** 25th–75th (IQR), **(c,f,i)** 90th (P90) percentile. The values represent the normalized density for each distribution.~~

~~We combine the percentile locations of the indices (P90, P10) to assess the aggregated distribution of organisation~~ To evaluate how the relationships between organisation indices and cloud/core properties evolve along the two seasonal subsets, we compare correlation coefficients in spring (MAM) and summer (JJA). ~~Averaged over the AOI, a high degree of convective organisation occurs most frequently between 15° S and 15° N. Over the ocean, convective organisation is higher during spring in the southern hemisphere and summerin the northern hemisphere. Over land, it is stronger over the northern hemisphere in summer. Our findings suggest that convective organisation is connected to vertical and horizontal cloud~~ Overall, SCAI maintains negative correlations with cloud properties, while COP and ROME remain positively correlated. The direction of correlation does not change along the period, though some coefficients vary in strength. From spring to summer, correlations between SCAI and cloud properties increase slightly - except for the CTH and core height. Correlations between COP and cloud properties predominantly increase, whereas the differences are lower than for SCAI. For ROME, we see an increase for the correlation to the cloud lifetime, CTH, and core height, and a decrease to the cloud area and core area. However, these shifts are small, with changes up to 0.11 (SCAI vs. cloud lifetime, CTH, and core height). Despite apparent spatial patterns and temporal shifts in convective cloud organisation and structure as seen in Figs. 8 and 9, statistical relationships remain overall weak (Table 4). These weak correlations suggest that these properties are influenced by additional regional factors beyond what the indices capture directly.

4.4 Investigating effects of convective organisation

To identify regional patterns of convective organisation and ~~core properties. A higher degree of organisation comes along an intense convective activity, a larger anvil area~~ their effects on cloud properties, we adopt a percentile-driven approach.

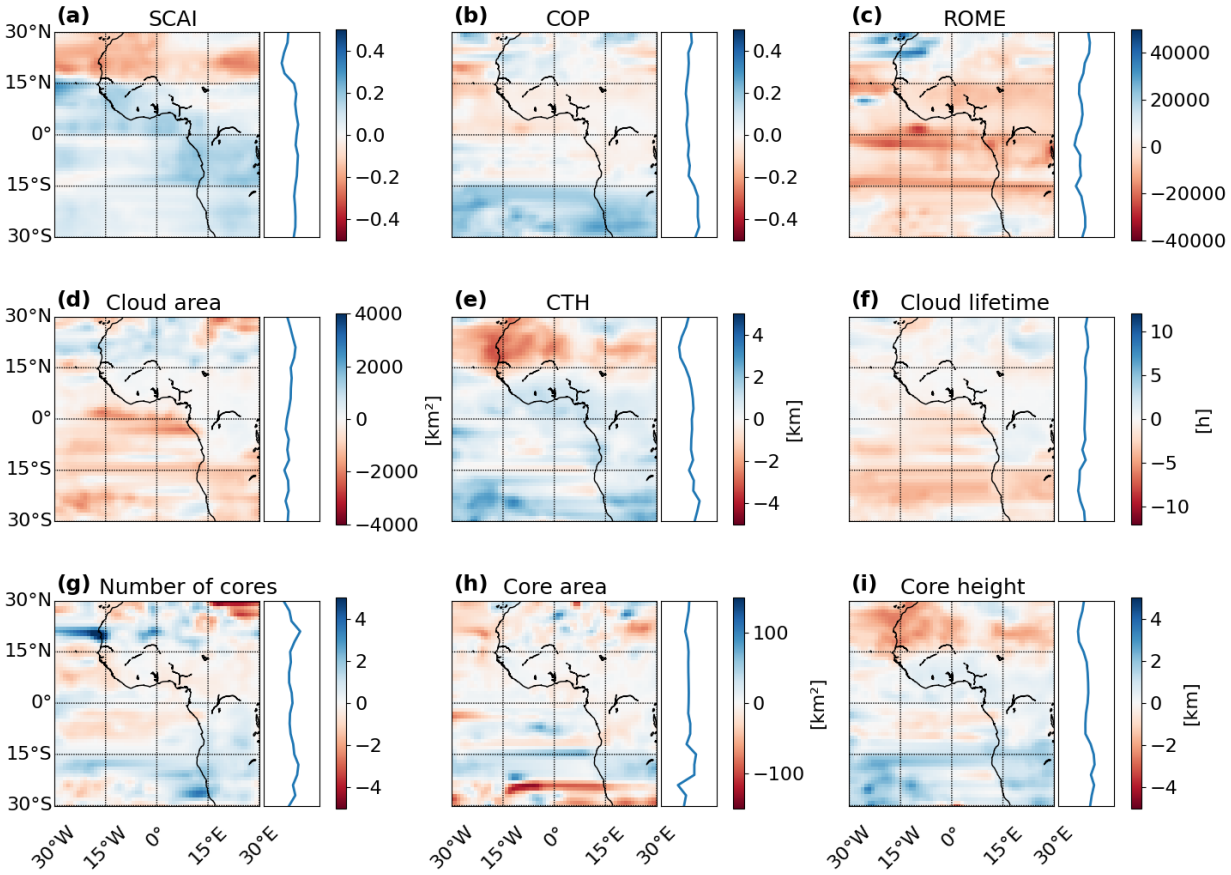

Figure 9. ~~Spatial distribution of convective organisation indices~~ Seasonal differences between ~~March and May~~ spring (MAM, n = 212,984) and summer (JJA, n = 141,089) values for ~~the~~ **(a)** SCAI, **(b)** COP, ~~SCAI~~**(c)** ROME, **(d)** the cloud area, **(e)** the CTH, **(f)** the cloud lifetime, **(g)** the number of cores, **(h)** the convective core size, and ~~ROME~~**(f)** the core height. ~~Data points are~~ The plot shows the spatial distribution in the AOI interpolated on a 3~~°~~ ° x 3~~°~~ ° grid ~~. Clouds are grouped as strong or weak organised using the **(a,d,g)** 10th (P10~~left) ~~, **(b,e,h)** 25th–75th (IQR), **(c,f,i)** 90th (P90) percentile. The values represent~~ and the ~~normalized density~~ average value for each ~~distribution~~latitude between 30° N and 30° S (right).

Table 4. Spearman's R for the SCAI, COP, and ROME against the cloud area, the cloud lifetime, the CTH, the number of cores, the convective core size, and the core height. The table shows the correlation coefficient for spring (MAM) and summer (JJA) and the seasonal difference.

	SCAI			COP			ROME		
	MAM	JJA	Difference	MAM	JJA	Difference	MAM	JJA	Difference
Cloud area	-0.06	-0.13	0.07	0.12	0.12	0.00	0.09	0.07	0.02
Cloud lifetime	-0.01	-0.12	0.11	0.05	0.10	-0.05	0.08	0.11	-0.03
CTH	0.24	0.12	0.11	0.04	0.07	-0.03	0.04	0.07	-0.03
Number of cores	-0.04	-0.08	0.05	0.07	0.09	-0.02	0.05	0.05	0.0
Core area	-0.04	-0.04	0.00	0.02	0.01	0.01	0.01	-0.03	0.02
Core height	0.12	-0.01	0.11	0.05	0.08	-0.03	0.05	0.07	-0.02

There exist no universally defined thresholds to distinguish between weak and strong convective organisation. In response, we compute the 10th, 25th, ~~a longer lifetime, and a lower area ratio (Section **??**). In spring, organised cloud systems primarily appear over the Atlantic Ocean and coastal Africa in the southern hemisphere. A second peak reflects the occurrence of oceanic MCSs between 15–30° S (Figure 11, a). We find the weakest organisation over the rainforest and the Atlantic Ocean near the equator (Figure 11, b). In summer, the hotspot locations shift northward. Then, we observe the highest number of organised clouds over the tropical Atlantic Ocean between 0°–15° N. A second peak persists over continental West Africa, the Jos Plateau, and the Congo River.~~

~~Along the AOI, the concurrent existence of weakly organised or isolated clouds and highly clustered cloud systems induces hotspots of~~ 75th, and 90th percentiles based on the distribution of each organisation index (SCAI, COP, and ROME) using the cloud tracks between March to August 2019 (Table 5). These percentiles serve as thresholds to classify the data into subsets of weak and strong convective organisation~~that occur in the same area (Figure 5, a–d). They may balance each other out, blurring derived spatio-temporal statistics. The location of this superimposition changes with the season. As shown in Sect. **??**, convective activity is marked by a high variability, especially over oceanic regions . Moreover, we find ambiguous results regarding convective organisation for different hemispheres, surface types, and seasons. These variations may be due to seasonal effects such as the northward shift of the ITCZ (Futyan and Genio, 2007), (Atiah et al., 2023). As shown in Part 1 of this study (Brüning and Tost, 2025), regional effects may alter the convective life-cycle. Although we observe a slightly stronger average organisation over the sea (Figure 4) , the analysis points out the complexity of deriving distinct patterns of convective organisation.~~ as induced by the interpretation of the indices: strong organisation may be related to low SCAI and high COP/ROME, weak organisation to high SCAI and low COP/ROME (Biagioli and Tompkins, 2023; Semie and Bony, 2020). Following, regions of strong convective organisation are defined as cloud tracks with an index value below the 10th percentile for SCAI or above the 90th percentile for COP and ROME. Conversely, regions of weak organisation correspond to values that lie above the 90th percentile for SCAI or below the 10th percentile for COP and ROME. To identify spatial and temporal

Table 5. Percentiles for the organisation indices (SCAI, COP, ROME) derived from the time series between March and August 2019. The table contains the percentiles Q10, Q25, Q75, and Q90 which are used as thresholds to filter subsets of strong or weak convective organisation.

	Q10	Q25	Q75	Q90
SCAI	0.165	0.224	0.418	0.528
COP	0.237	0.278	0.381	0.443
ROME	3260.327	5652.496	14695.356	22659.608

patterns of convective organisation, we create two subsets from all data points in the dataset, whereas one represents the 10 % strongest convective organisation (Q10 for SCAI; Q90 for COP and ROME, hereafter: P90), and the other representing the 10 % weakest convective organisation (Q90 for SCAI; Q10 for COP and ROME, hereafter: P10). These may represent so-called "hotspots". We also define the interquartile range (IQR, values between the 25th–75th percentile) to represent a baseline, which is used to contrast the spatial distribution of average organisation against the identified hotspot regions.

~~Spatial distribution of convective organisation indices computed by aggregating percentiles of COP, SCAI, and ROME for the months March to May (MAM, upper row) and June to August (JJA, lower row). Clouds are grouped as the **(a) & (c)** most organised or **(b) & (d)** the least organised using the 10 % lowest (SCAI) or highest (COP, ROME) data points. The values represent the normalized density for each distribution interpolated on a 3° x 3° grid.~~

4.5 ~~Seasonal effects on convective organisation~~

~~The seasonal analysis of the organisation indices emphasises a connection between a pronounced convective organisation, the hemisphere, and the surface type (Figure 12). Between March and August, COP and ROME increase in the northern hemisphere . At the same time, we observe ambiguous results for SCAI, with a slight increase over land~~

4.4.1 Characteristics of percentile-based subsets

We filter the dataset by the percentiles from Table 5 to create the subsets of weak (P10) and strong (P90) convective organisation. Both subsets include 84,132 samples. Our analysis reveals that the frequency and location of convective clouds — and their strength of organisation — are not evenly distributed spatially or temporal. The majority of cloud tracks was detected between 10° S and 20° N (Figure 2). However, we observe distinct temporal and land–sea contrasts reflected in both P90 and ~~a decrease over the ocean (Figure 12, a–c). Differences between the surface types comprise up to~~ P10. During March–May (MAM), strong convective organisation (P90) is more prevalent over land in the southern hemisphere and over ocean regions between 10°–30° S and 5~~% (COP, ROME) and ~~° S–10° N. From June–August (JJA), P90 occurrences shift northward, peaking over land between 10~~% (SCAI) of the index scale. Over the southern hemisphere, the indices show a higher variability (Figure 12, d–f). We detect a tendency for stronger organisation in the southern hemisphere accompanied by a higher cloud anvil area, cloud lifetime and enhanced core size but reduced CTH (Figure 7). For COP and ROME, we find an increase between March~~

~~Seasonal changes of the organisation indices in the AOI between March and August 2019 grouped by the hemisphere. We show **(a,d)** the COP, **(b,c)** the SCAI, and **(e,f)** the ROME on the northern (NH, upper row) and southern (SH, lower row) hemisphere over land and sea. We visualise the monthly mean (solid lines) and the 7-day rolling mean (dashed lines).~~

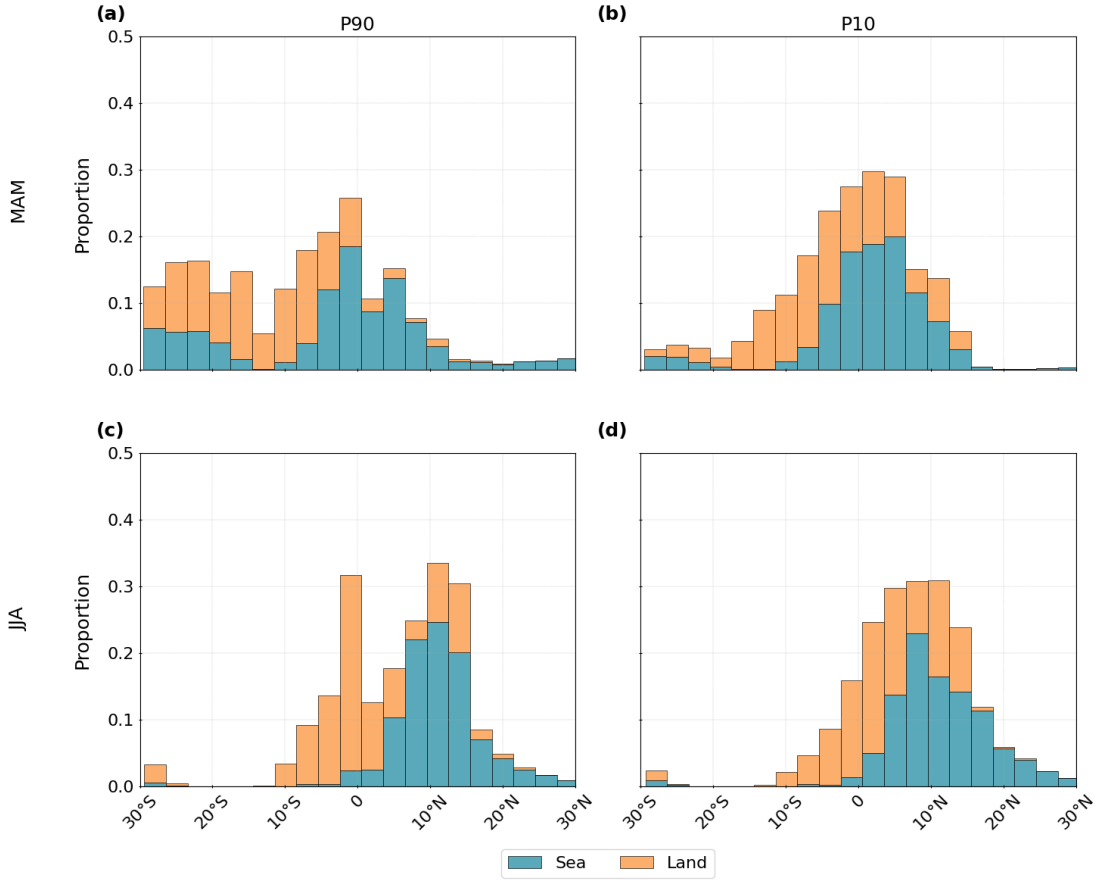

Figure 10. Distribution of detected clouds grouped in 3° intervals between 30° S and 30° N. The histograms show the proportions of cloud tracks grouped by the surface type (land, sea) for **(a)** the 10 % strongest convective organisation (P90, n = 84,132) and **(b)** the 10 % weakest convective organisation (P10, n = 84,132) between March–May (MAM) and June–August (JJA).

~~and May, followed by a minimum in June and a renewed increase between July and August. The values of SCAI show a linear decrease from spring to summer. There is a weak to moderate trend towards higher (COP, ROME) or lower (SCAI)index values during summer in the northern hemisphere. In the southern hemisphere, we see an increase in convective organisation over the ocean and a decrease over land.~~ ° S–5° N and over ocean between 5°–15° N. A persistent local minimum appears around 0°–5° N in both seasons (Figure 10, a, c). In contrast, weak convective organisation (P10) is rare north of 15° N in spring and south of 15° S in summer. In MAM, it is more frequent over land from 10° S–10° N and over ocean between 0°–10° N. In JJA, we see an overall northward shift of the distribution (Figure 10, b, d).

~~In Sect. 4.2, we have detected a high spatial variability that modifies regional convective cloud development and organisation patterns. Further, we investigate seasonal differences for cloud and core properties for strongly (~~

Comparing the dataset with all cloud tracks and the percentile subsets, we observe that strong convective organisation occurs about 15 % more frequently over ocean, while cloud systems with a weak convective organisation are more common over land (Figure 11, a). P10 clouds are generally associated with fewer cores and shorter lifetimes than both P90 and the full dataset. They may be associated to a higher proportion to single-core clouds (15 % higher than P90) and clouds with a lifetime between 0–3 h (30 % higher than P90). We observe more clouds from P90 with a cloud lifetime of more than 3 hours. However, the longest lifetimes in the dataset may be found for clouds not connected to the percentile subsets (Figure 11, b, d). Clouds were detected slightly more frequently in MAM than JJA. In March, the proportion is especially high for P10 (15 % higher than P90)~~and weakly (~~. In contrast, occurrences of P90 are less common in MAM and increase in JJA (10 % higher than P10)~~organised cloud clusters. Following an overall slight increase of convective organisation in~~ . These findings may indicate an increase of strong convective organisation during boreal summer (Figure ~~12), we also see a weak trend towards more and larger DCCs (Figure 13) . Overall, organised clouds~~ 11, c).

4.4.2 Relationship between organisation subsets and cloud properties

To explore how the relationship between cloud and core properties differs for weak (P10) and strong (P90) ~~come along a larger cloud anvil area, a longer cloud lifetime, a lower CTH, a lower area ratio, and more and larger DCCs. This pattern appears mainly in the northern hemisphere during summer. However, there is a high spatial variability (Section 4.2). For example, in summer, we observe extensive, long-lasting, and more clustered clouds north of the equator (< 15° N). At the same time, convective activity decreases over the Sahel (> 15° N) (~~convective organisation, we compare the correlation coefficients between all cloud tracks and the two subsets. As noted in Sect. 4.2, SCAI tends to correlate negatively with cloud properties, while COP and ROME show positive associations. For all cloud tracks, correlations between the indices range from -0.08 to 0.26 (Figure 7). ~~Strong and weak convective organisation is more similar in the southern hemisphere than in the northern hemisphere~~Figure 12 highlights that inter-index and intra-cloud property correlations are stronger than those between indices and cloud properties. Here, ~~we see aweak trend towards smaller and less clustered clouds in the 90th percentile. For weakly organised clouds (P10), we detect more ambiguous results in both hemispheres. These clouds come with a decrease in the~~ COP and ROME exhibit moderate to strong positive correlation, while COP and SCAI are moderately negatively correlated (Figure 12, a). SCAI and ROME show a weak to moderate inverse relationship. Among cloud and core properties, the strongest positive correlation is between cloud area and number of cores, followed by CTH and core height. The number of cores, core area, and core height are also moderately correlated. Cloud lifetime, however, shows only weak to moderate associations with these properties. In the P90 subset, all three indices are positively correlated - a departure from the expected negative SCAI–COP/ROME relationship seen for all cloud tracks. Correlations between cloud and core properties in P90 remain largely similar to the full dataset, though some relationships (e.g., between COP/ROME and core height or area) strengthen slightly (Figure 12, b). In P10, we find similar property-to-property correlations, though the strength varies more. The strongest correlation remains between the number of cores and core area and the core and cloud height (Figure 12, c).

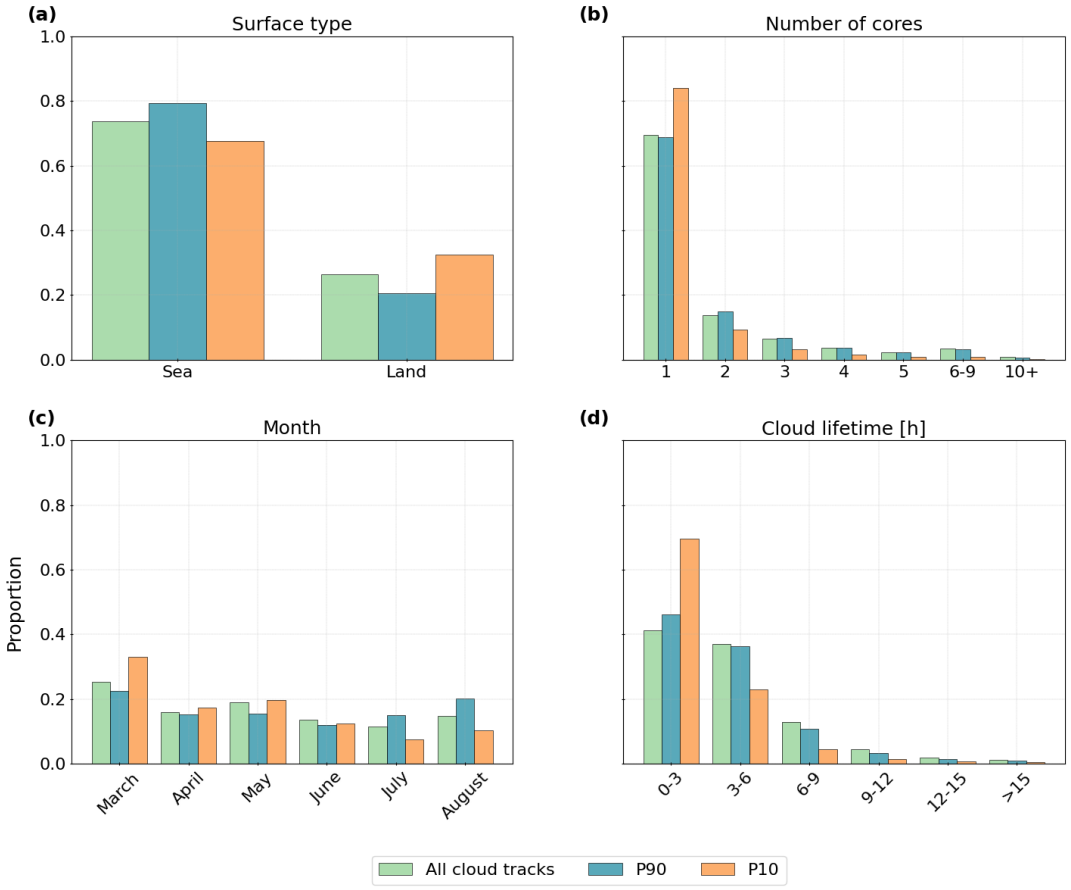

Figure 11. Comparison of the distributions between all cloud tracks, the 10 % strongest convective organisation (P90), and the 10 % weakest convective organisation (P10) for **(a)** the surface type derived from a land-sea mask, **(b)** the number of cores, **(c)** the month, and **(d)** the cloud lifetime after first detection.

For all data, we remain to find the strongest correlation between SCAI for the indices and CTH for the cloud~~lifetime and the number of associated DCCs in summer, whereas the DCC size and CTH increase.~~ /core properties. Uniquely, SCAI and ROME show a high positive correlation in both P10 and P90, despite being theoretically opposed in their interpretation of convective organisation (Section 3, Section 4.1). This apparent contradiction underscores the complexity of the indices, particularly when filtered by percentiles.

~~In the following section, we examine the statistical significance of the seasonal differences for organised cloud clusters (~~

To assess whether differences between datasets are statistically significant, we compare parameter distributions for all cloud tracks, P90~~). For this purpose, we divide the 29 365 cloud clusters into four groups based on the surface type (Sea, Land) and the season (MAM, JJA). The group sizes in our study are imbalanced since more clouds occur over the ocean (Brüning and Tost, 2025). To detect statistically significant differences between the group mean values, we~~ , and P10 subsets.

~~Seasonal changes of the convective cloud and core properties between March and August 2019 grouped by the hemisphere. We see the monthly mean for the 90th (P90, n = 29 365) and 10th (P10, n = 30 243) percentile of **(a)** the cloud anvil area, **(b)** the CTH, **(c)** the cloud lifetime, **(d)** the number of DCCs, **(e)** the convective core area, and **(f)** the area ratio between cloud anvil and core area on the northern (NH) and southern (SH) hemisphere.~~

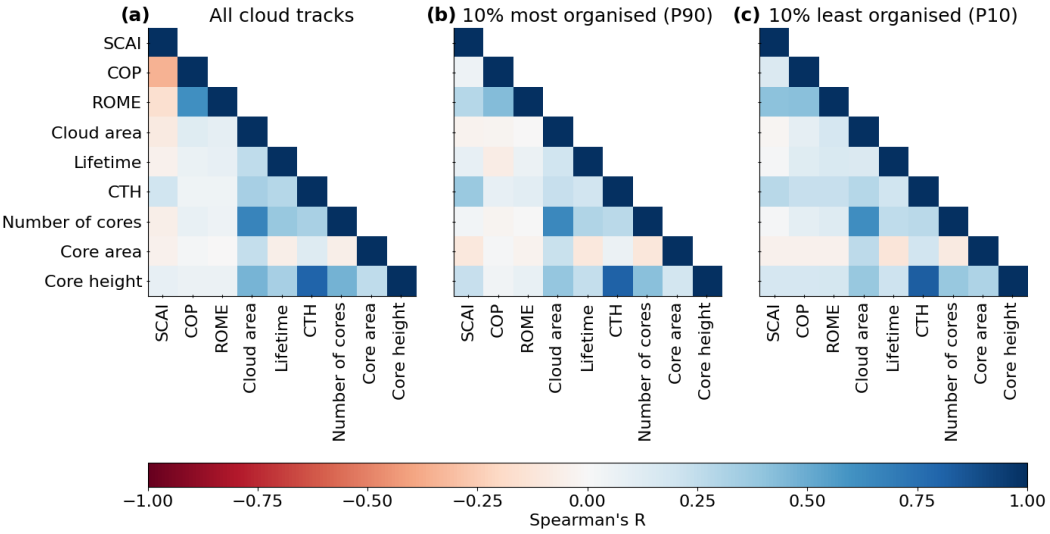

Figure 12. Correlation matrix for the organisation indices, cloud and core properties. We calculate Spearman's R to quantify the correlation coefficient on a scale between -1 and 1 for **(a)** the whole dataset of cloud tracks (n = 354,073), **(b)** the 10 % most organised clouds (P90, n = 84,132), and **(c)** the 10 % least organised clouds (P10, n = 84,132).

We apply Welch's t-test~~for independent samples. In contrast to the Student's t-test, the results remain robust for skewed distributions and large or uneven~~ , which may be more robust for unequal sample sizes (Derrick and White, 2016). ~~Moreover, we calculate~~ For instance, we complement this with Cohen's D to ~~complement the t-test results. It measures the difference between two means based on standard deviation units (effect size). Large values of Cohen's D indicate the difference between the means is higher than the variability (Cohen, 2013). The effect size is positive and ranges between 0 and infinity, with a classification indicating~~ estimate the effect size as small (< 0.2), medium (0.2–0.5), or large (≥ higher than 0.8) ~~differences.~~

~~We see an overall shift of the indices' distribution towards a stronger organisation during summer (JJA) (Figure 12, 14 a–c). For COP, we find the highest~~ (Cohen, 2013). The organisation indices show statistically significant differences across the three subsets, with large effect sizes for SCAI, COP, and ROME. Here, the effect size is largest between all data and P10 (Figure 13, a–c). Cloud and core properties exhibit more nuanced differences. The cloud area shows the largest effect size between ~~oceanic and continental surfaces in summer and the lowest in spring. The seasonal differences are generally higher over land than the ocean. Although the p-values point out statistically significant differences between the means of the distribution, we detect a predominately small effect size. For SCAI, we find higher values and a larger effect size in summer (JJA) (Figure 12). Although~~

Table 6. Summary of differences between cloud and core properties for all cloud tracks against the percentile-based classification of weak (P10) and strong (P90) convective organisation. The table contains the arithmetic mean of all properties for the three datasets. We show in which direction the subset mean differs from all tracks (Direction) and the effect strength (Cohen's D) for all tracks compared to P90 or P10.

	All tracks		P90		P10		
	Arithmetic mean	Direction	Arithmetic mean	Cohen's D	Direction	Arithmetic mean	Cohen's D
SCAI	0.331	-	0.198	large	+	0.433	large
COP	0.334	+	0.449	large	-	0.240	large
ROME ~~is~~	11858.977	+	24274.897	large	-	4413.081	large
Cloud area	421.225	+	485.431	small	-	223.537	medium
CTH	16.077	-	15.696	medium	-	15.755	small
Cloud lifetime	4.119	-	3.691	small	-	2.501	medium
Number of cores	1.774	-	1.740	small	-	1.305	medium
Core area	44.976	+	50.074	small	+	47.636	small
Core height	10.704	-	10.428	small	-	10.266	small

~~the arithmetic mean of SCAI is similar over both surface types, the IQR shows a broader value range over land (Figure 14, a–c) . The effect size for~~ all data and P10, while the CTH shows higher differences between all data and P90 (Figure 13, d, e). Compared to all cloud tracks, P90 clouds tend to be larger, with lower CTH, slightly shorter lifetimes, and slightly less, larger, and lower cores. P10 clouds are smaller, with a higher CTH, shorter lifetimes, fewer cores, and a larger core area and lower core height than clouds in the full dataset (Figure 13, d–i). For the number of cores, we find very low differences between all data and P90. As seen in Fig. 2, single-core clouds dominate the dataset. This skewness may affect statistics - in particular of data in P10 - which are heavily weighted toward fewer cores. Core area is larger in P90 and P10, whereas core height is lower in P90 and P10. However, for the core area, we observe only very small differences between the subsets (Figure 13, f–i).

While we detect statistically significant differences between percentile-based subsets and the dataset with all cloud tracks, the effect sizes for cloud and core properties remain mostly small to moderate. Our results indicate that strong convective organisation (low SCAI, high COP and ROME) tends to co-occur with larger cloud and core areas, slightly less and lower cores, and slightly shorter lifetimes. The highest effect sizes may be found for the CTH, core height, and cloud lifetime. Weak organisation (high SCAI, low COP and ROME) is associated with smaller clouds, lower CTH, fewer cores, a smaller core area, lower core height, and shorter lifetimes. Here, we observe the highest effect sizes for the cloud area, number of cores, and cloud lifetime (Table 6). These findings - and the differences between the two percentile-based subsets - suggest that different aspects of cloud and core morphology may contribute to the strength of convective organisation.

4.4.3 Spatial distribution of percentiles

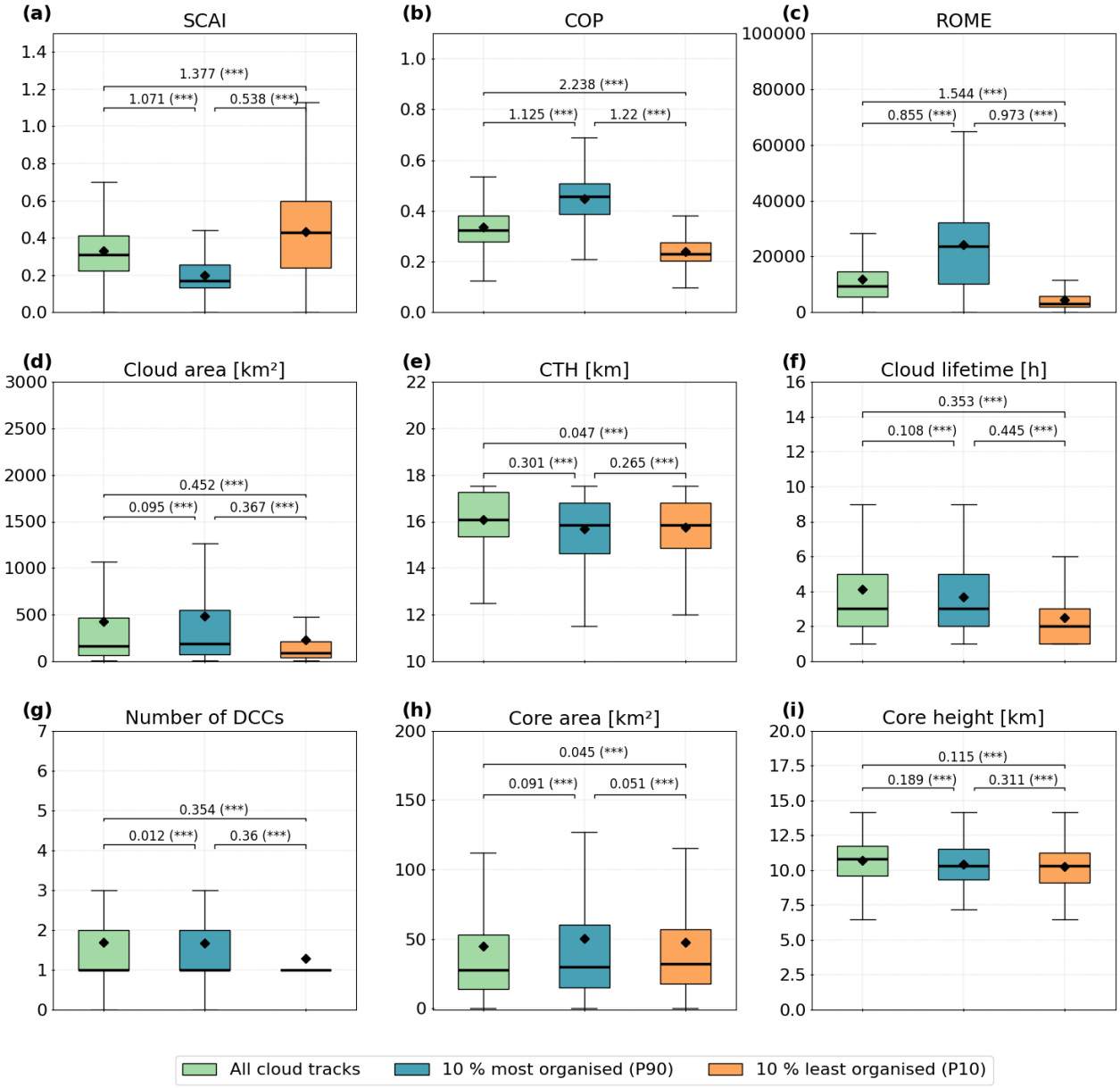

Figure 13. Boxplot showing the distribution of the convective organistaion indices, cloud and core properties for the whole dataset (n = 354,073), the 10 % most organised clouds (P90, n = 84,132), and the 10 % least organised clouds (P10, n = 84,132). We show the distribution of **(a)** the SCAI, **(b)** the COP, **(c)** the ROME, **(d)** the cloud area, **(e)** the CTH, **(f)** the cloud lifetime, **(g)** the number of cores, **(h)** the convective core area, and **(i)** the core height. The boxplot contains the median (bold black lines) and the arithmetic mean (black diamonds). Annotations depict the effect size measured by Cohen's D and the p-value derived from Welch's t-test (not significant (ns): p higher than 0.1, significant with *: $p < 0.1$, **: $p < 0.05$, ***: $p < 0.01$).

To identify how convective organisation may be spatially distributed for each of the three organisation indices (SCAI, COP, ROME), we filter the dataset of all cloud tracks by the percentiles (Q10, ~~on average, higher than for COP and SCAI. Again, the distribution shifts towards higher averages in summer. Our analysis emphasises the importance of seasonal and spatial effects on cloud organisation. For instance, we detect statistically significant differences between organised convection in spring (MAM)and summer (JJA) over land and sea ($p < 0.05$) . The distributions of COP and ROME show a noticeable narrowing in summer (JJA). However, the effect size suggests the differences are relatively small, except for ROME and SCAI over land.~~

~~The distribution of the cloud area, the cloud lifetime,~~ Q90) and ~~the core size slightly shift in summer. We observe a broadening over the ocean and a narrowing over land, whereas the median remains similar~~ we map the frequency of cloud occurrences across the area of interest (AOI) between 30° N–30° S and 30° W – 30° E. The data is interpolated using a 3° × 3° grid and smoothed with a Gaussian filter (sigma = 0.5). In addition to the percentiles Q10 and Q90, we visualise the interquartile range (IQR; 25th–75th percentile) for each organisation index. Frequency values (0–140 per grid cell) are colour-coded to represent absolute counts.

As shown in Sects. 4.1 and 4.2, high SCAI values - indicating weak convective organisation - are typically concentrated near the equator. In spring, low SCAI values (Q10) occur over the equatorial Atlantic Ocean and land/sea areas south of 15° S. High values (Q90) appear over equatorial Africa (0°–15° N), especially in rainforest zones, and Cameroon. The IQR peaks near the equator, particularly over the Ivory Coast, Guinea, Benin, Angola's coast, and Lake Victoria (Figure 14, a–c). In summer, values shift north to 0°–15° N, with SCAI Q10 regions over the Atlantic and coastal West Africa. High SCAI (Q90) values occur in spring over the Congo and Central African Republic. The IQR also shifts north in summer, with hotspots over the West African plains, Jos Plateau, and Congo River basin (Figure 15, a–c). COP exhibits weaker spatial variability than SCAI or ROME. We detect clusters of low (Q10) COP near the equator in both seasons, over the Atlantic in spring and across continental Africa in summer. For high values (Q90) in spring, strong peaks are found along West and Central African coasts and offshore in the Atlantic Ocean - many overlapping with regions of low COP, suggesting coexisting weak and strong organisation (Figure 14, ~~d, f, h). Following, we observe only a small effect size. The seasonal variability of the CTH is weaker, particularly over the ocean. Contrasting, we observe higher values of the CTH in summer~~d–f). In summer, peaks of high COP (Q90) are concentrated over the Atlantic Ocean near Cape Verde and coastal zones between Senegal and Sierra Leone. Secondary peaks appear inland across West Africa (Figure 15, d–f). The IQR aligns closely around the equator but shifts northward in summer, with dominant peaks over Central Africa's rainforest and minor peaks across the West African plains (Figures 14 b, e, 15, b, e). ROME shows greater latitudinal variability than SCAI and COP. In spring, low values (Q10) values focus primarily along 15°–30° W near the equator, and secondarily between 15° S–15° N. High values (Q90) values are concentrated along the West African coast and between Cameroon and Gabon. IQR peaks are dispersed over the equatorial rainforest and coastlines (~~JJA). Accordingly, the effect size between the groups over land and sea is enhanced. We find a similar seasonal pattern for the number of DCCs and the area ratio (~~Figure 14, ~~g, i). However, the effect sizes remain small and suggest only a weaker seasonality for the number of DCCs and the area ratio.~~ g–i). In summer, low ROME (Q10) clusters around the Congo River and more diffusely across continental Africa. Peaks for high values of ROME (Q90) appear over the Jos Plateau, Congo River, and Atlantic. Like COP,

ROME shows overlapping regions of weak and strong organisation over rainforests and oceans. IQR values peak between 0°–15° N and extend to coastal West Africa (Figure 15, g–i).

The spatial patterns of COP and ROME are closely aligned, with the 10th and 90th percentiles showing often spatial overlaps. SCAI has an inverse pattern due to its opposing index scale: regions with high COP/ROME may correspond to low SCAI (and vice versa). This inverse relationship is evident throughout the period, with all three indices exhibit consistent spatial patterns. The IQR maps, consistent across indices, reveal a northward shift of the indices which aligns with convective cloud occurrences during summer as depicted for the percentile-based subsets in Fig. 10.

~~To summarise, the frequency of convective activity and, for instance, the strength of convective organisation increases in the northern hemisphere from spring to summer~~

4.4.4 Identifying hotspots of convective organisation

In contrast to the former analysis, we examine the spatial distribution for clouds in the two subsets (P90, P10) (Section 4). These subsets of the 10 % strongest (P90) and the 10 % weakest (P10) convective organisation may help to identify cumulative hotspot regions averaged over the three indices. The data may allow us to analyse spatial patterns and temporal changes of convective organisation across two seasons from spring (March to May, MAM) to summer (June to August, JJA). The occurrences are interpolated onto a 3° × 3° grid between 30° N–30° S and 30° W–30° E and smoothed using a Gaussian filter with a kernel size of 0.5. ~~In contrast, convective organisation in the southern hemisphere is more pronounced in spring. Compared to the northern hemisphere, the properties of convective clouds and cores are more similar for strong and weak convective organisation~~

In spring, the highest proportion of strong convective organisation (P90) occurs over the Atlantic Ocean, with a notable concentration near the equator and between 15° and 30° S. Additional hotspots are found along the West African coastlines, the Gulf of Guinea. Moreover, we observe small peaks over the equatorial rainforest, Angola, and parts of the Sahel. Overall, most of the data points for the 10 % strongest convective organisation during spring are located south of the equator (Figure 16, a). Weak convective organisation during spring displays two primary clusters. The first is located over the equatorial Atlantic Ocean, particularly between 15° and 30° W. The second spans continental Africa, where more dispersed peaks emerge between Cameroon and the ~~southern hemisphere has a higher variability concerning the organisation indices and the frequency of intense convective activity. Regions with different degrees of convective organisation show partly ambiguous results for the associated cloud properties, especially for the core size and CTH. While we find statistically significant differences between organised convection based on spatial and temporal factors, the strength of these effects is predominately small. The derived differences in the distributions may not be sufficient to explain the spatio-temporal variability of the patterns we detected in Sect. 4.2. However, the total of detected uncertainties and limitations reflect the complexity in quantifying convective organisation .~~

5 ~~Discussion~~

~~According to results by Stubenrauch et al. (2023),~~ Congo River. Across the belt from 15° N to 15° S, the frequency of the 10 % weakest convective organisation is generally high (Figure 16, b). In summer, the spatial distribution of strong convective

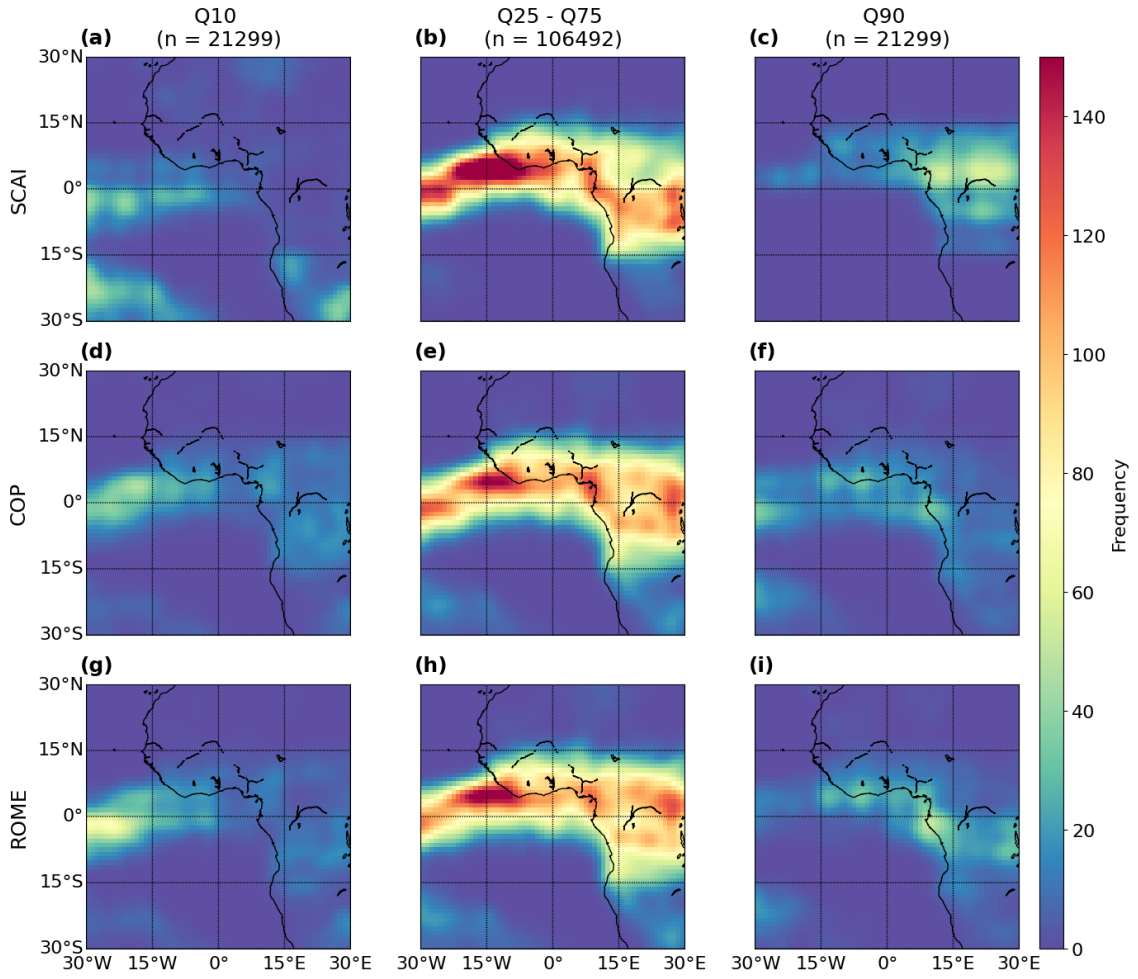

Figure 14. ~~Boxplot for organised cloud clusters (P90, n = 29 365) grouped by~~ Spatial distribution of the ~~surface type (Sea~~percentiles Q10, ~~Land) and season (MAM~~Q25–Q75, ~~JJA). We show **(a)**~~ and Q90 for the ~~COP, **(b)** the~~ convective organisation indices **(a–c)** SCAI, ~~**(c)** the ROME~~**(d–f)** COP, ~~**(d)** the cloud anvil area, **(e)** the CTH, **(f)** the cloud lifetime, **(g)** the number of DCCs, **(h)** the convective core area,~~ and ~~**(i)** the area ratio~~ **(g–i)** ROME between ~~cloud anvil~~ March and ~~core area. The boxplot contains the median~~ May ~~(bold black lines) and the arithmetic mean (black diamonds). Annotations depict the effect size measured by Cohen's D and the p-value derived from Welch's t-test (not significant (ns): $p \geq 0.1$~~MAM, ~~significant with *: $p < 0.1$~~n = 212, ~~**: $p < 0.05$, ***: $p < 0.01$~~984). The values represent the frequency distribution interpolated on a 3° x 3° grid.

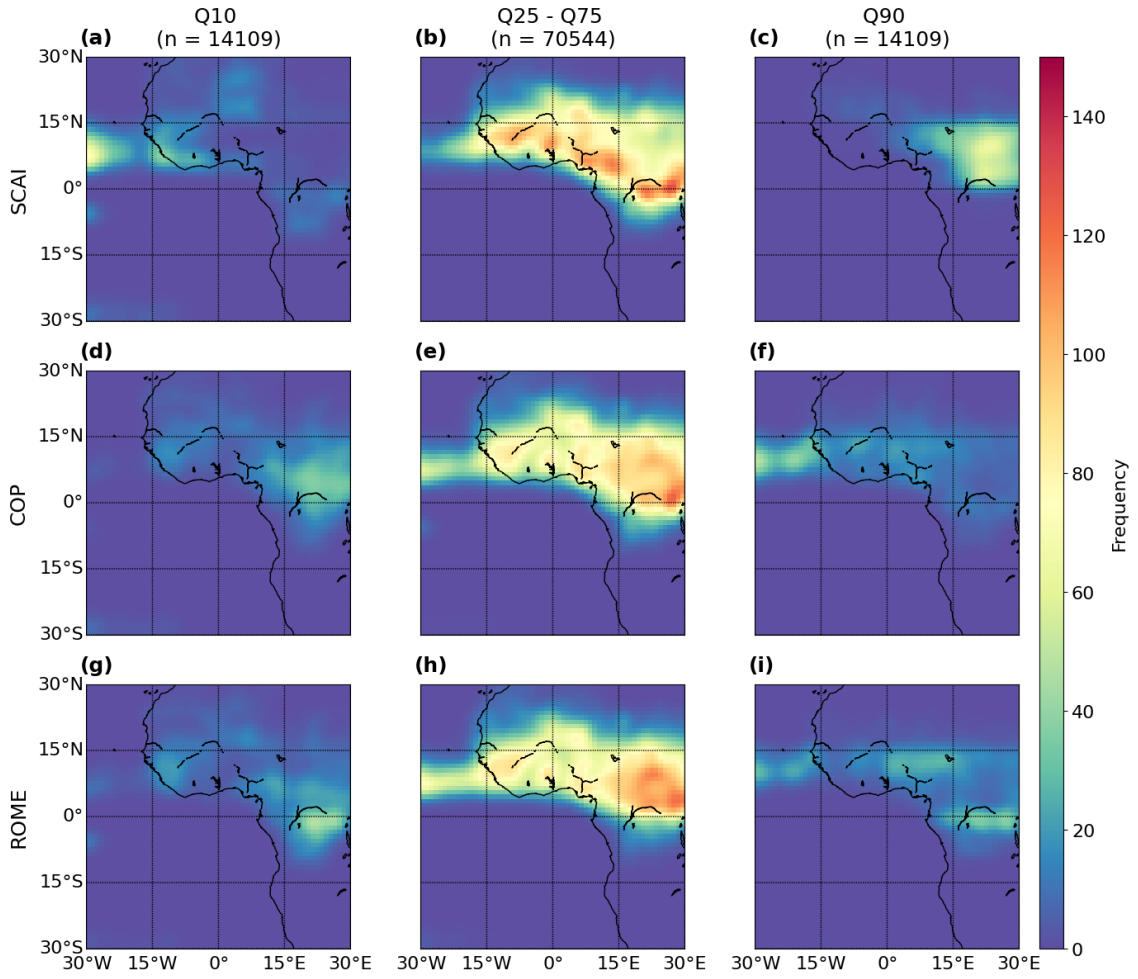

Figure 15. Spatial distribution of the percentiles Q10, Q25 - Q75, and Q90 for the convective organisation indices **(a–c)** SCAI, **(d–f)** COP, and **(g–i)** ROME between June and August (JJA, n = 141,089). The values represent the frequency distribution interpolated on a 3° x 3° grid.

organisation ~~is associated with larger, more clustered convective systems (Section 4.1). We find a connection between the spatio-temporal variability of convective organisation and the microphysical cloud properties such as the cloud anvil area, the CTH, or the cloud lifetime (Bläckberg and Singh, 2022). In our study, organisationindices vary with the cluster size, cloud lifetime, and the ratio between the DCCs and the anvil area (Section 4.1, **??**). MCSs with a lower area ratio appear as more organised (Section **??**). Within clustered clouds like MCSs, interactions between DCCs may enhance the convective activity and prolong the cloud lifetime, anvil growth, and vertical updraft strength (Tompkins and Semie, 2017). In contrast to previous results (Takahashi et al., 2017; Stubenrauch et al., 2023), we detect a slightly stronger organisation~~ shifts northward. Regions with a frequent occurrence of strong convective organisation emerge over the Atlantic Ocean and become more widespread across the West African plains, including areas around the Niger and Congo rivers (Figure 16, c). Weak organisation, on the other hand, is concentrated primarily over continental Africa, especially between 15° and 30° E, with a peak located just north of the Congo River (Figure 16, d).

As suggested in Sect. 4.4.3, we observe overlapping regions of weak and strong convective organisation throughout the period. In spring, this overlap is evident over both ocean and land, whereas in summer, it is mainly confined to continental Africa. Overall, cloud occurrences and spatial patterns suggest a shift between MAM and JJA which is consistent to the imbalance between cloud tracks over land and ocean observed in Fig. 11. In spring, strong convective organisation is more frequently observed over the ocean, ~~which may be due to the dominance of oceanic clouds in our study (Section 4.1). Moreover~~while weak organisation is distributed across both land and sea. By summer, strong organisation becomes more prominent over land, and weak organisation is largely confined to the African continent. This migration of convective hotspots appears consistent with the northward movement of the ITCZ, as described in Atiah et al. (2023).

5 Discussion

5.1 Summary of key findings

Our analysis reveals that convective cloud occurrence and convective organisation vary considerably across both space and time. While the study spans only six months and does not provide a full climatology, the results ~~may reflect an extensive transport of continental convective clusters towards the ocean (Vondou, 2012). The differences over land and sea account for about 10 %, which is lower than the seasonal difference of about 15–20 % . A higher seasonal variability of convective activity in the southern hemisphere is associated to a more fluctuating strength of organisation. However, the microphysical properties of weakly and strongly organised clouds are more similar than in the northern hemisphere. For continental cloud clusters in the northern hemisphere, we find more distinct results regarding the relationship between DCCs and the degree of organisation (Section **??**). Our results show that grouping organised cloud clusters by temporal and spatial factors like the season or surface type reveals statistically significant differences ($p < 0.05$)between the means of their distribution (Section **??**)~~ highlight spatial and temporal changes of convective organisation during the period. Notably, the frequency of the 10 % strongest convective organisation increases during the summer months (June to August), particularly north of the equator (Figure 11, Figure 16, c–d). In spring (March to May), it may occur more frequently south of the equator (Figure 16, a–b). Between March and May,

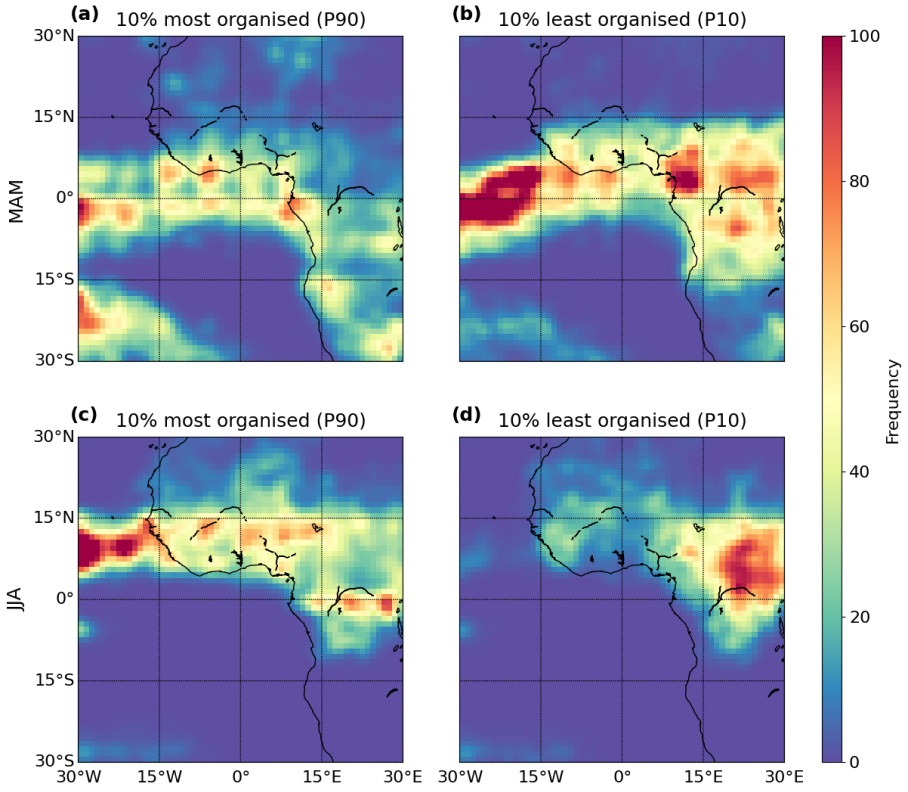

Figure 16. Spatial distribution of convective organisation based on an aggregation of the percentiles for SCAI, COP, and ROME in spring (MAM, upper row) and summer (JJA, lower row). Clouds are grouped as the **(a) & (c)** strong organised or **(b) & (d)** weak organised using Q10 lowest (SCAI) or Q90 (COP, ROME). The values represent the frequency distribution interpolated on a 3° x 3° grid.

we observe a higher concentration of strongly organised convection over the Atlantic Ocean, primarily between 0° and 30° S. This peak shifts northward to between 0° and 15° N in summer, with additional hotspots appearing over the equatorial rainforest and West Africa. Meanwhile, weakly organised convection tends to dominate over the Atlantic Ocean in spring and shifts to continental Africa in summer. These findings suggest a broader northward movement of convective cloud occurrences throughout the study period (Section 4.2, Section 4.4). ~~Nevertheless, the absolute difference for the convective cloud properties between these groups remains predominately small. Contrasting, we find a higher variability and a medium to high effect size for the organisation indices (Section 4.3). While the analysis helps to assess spatio-temporal patterns of convective organisation, further advancing the understanding of underlying processes may require the integration of additional properties. Moreover, a less skewed distribution for clouds over land and ocean may reduce the imbalance between group sizes and improve the robustness of statistics.~~

~~Our results emphasise that changes on multiple scales influence convective cloud organisation. When comparing spatial patterns, we see ambiguous results for organisation indices in the southern and northern hemispheres and between regions~~

near the equator and the tropics (Section Correlations between convective organisation indices (SCAI, COP, ROME) and cloud/core properties suggest generally weak to medium relationships for all cloud tracks. SCAI is negatively correlated to the properties, except for the CTH and core height, while COP and ROME show positive correlations except for the core area. In all cases, the coefficients remain below 0.3 (Section 4.2). Convective organisation may be driven by the interplay of processes induced by, e.g., local surface characteristics (Vondou, 2012), the monsoon circulation (Futyan and Genio, 2007), or the katabatic flow in mountainous regions (Nicholson, 2018). Narrowing down their effect on convective organisation requires further clarification. Moreover, we detect overlapping effects of weak and strong organisation that blur the statistical analysis (Section **??**These correlations partly change for the 10 % strongest and 10 % weakest convective organisation. Within these subsets, we find the highest corelation coefficient between SCAI and the CTH for clouds with a strong convective organisation. However, the relationships between the cloud and core properties remain similar over all subsets (Section 4.4.2). In contrast, we observe pronounced changes in both the indices and the associated cloud characteristics along the period and across the AOI. These changes reflect a high variability for average values, though the correlation strength remains limited (Section 4.3). The currently employed indices allow us to identify geographical patterns of large-scale cloud clustering. Nevertheless, further uncertainties persist. These comprise the impact of the terrain on cloud organisation and its connection to severe weather (Biagioli and Tompkins, 2023). A metric built simultaneously using more indices or integrating spatial and temporal factors in the calculation may enhance the results (Pscheidt et al., 2019). This study employs a grid-based approach with a moving window (Section 3.2). Before, numerous studies applied the idea of partitioning the AOI into subsets of an equal area (e.g., Tobin et al. (2012); Stubenrauch et al. (2023); Retsch et al. (2020)). While a moving window may prevent small-scale fluctuations between grid cells, it is still based on a somewhat arbitrary, human-induced splitdistribution of cloud and core properties within identified hotspot regions differ from those observed in the full dataset of all cloud tracks. We analyse the effect size using Cohen's D to reveal how organisation strength may influence cloud characteristics. Compared to all cloud tracks, the cloud systems of the 10 % strongest organisation tend to have larger cloud and core areas, a lower CTH and core height, a shorter lifetime, and a lower number of convective cores. In contrast, unsupervised clustering algorithms like DBSCAN or the improved HDBSCAN may provide a more data-driven approach. Zuo et al. (2022) used the DBSCAN algorithm to identify cloud clusters within 3D radar data. Furthermore, Kim et al. (2023) derived precipitation probabilities from geostationary satellite data with an unsupervised clustering technique. In our following work, we will investigate whether these algorithms are suitable to identify robust patterns of convective cloud organisationthrough space and timeweaker convective organisation may be typically associated with smaller clouds and larger cores, fewer cores, shorter lifetimes, and lower vertical extent. Strong convective organisation differs the most from all cloud tracks regarding the CTH and from weak organisation regarding the cloud lifetime. Between weak convective organisation and all cloud tracks, we identify the cloud area to have the highest effect size (Section 4.4.2). Hence, the cloud area appears to be more important to identify weak convective organisation, whereas strong convective organistaion may be stronger driven by the CTH. Despite these differences in the distribution of cloud and core properties, we detect partly the same direction for correlations in case of strong and weak convective organisation, highlighting the complexity of involved processes.

5.2 Spatio-temporal drivers of organisation

~~Referring to our findings from Part 1 of this paper sequence (Brüning and Tost, 2025), convective cloud development is subject to spatial and temporal changes. These effects come into play regionally and on a larger scale. We see a link between intense convective cores , extensive MCSs and the occurrence of~~ Our results show that convective organisation tends to be stronger for cloud properties typically associated with large convective systems containing multiple core regions, such as MCSs (Stubenrauch et al., 2023). In line with Brüning and Tost (2025), we observe that cloud area, lifetime, cloud top height (CTH), core area, and core height all grow with the number of convective cores (Figure 12). While multiple cores may enhance cloud longevity, promote cloud area growth, and strengthen vertical updrafts, the number of cores may also be a key factor in determining the strength of convective organisation. ~~In spring, we observe a weaker convective activity represented by smaller cloud anvils and fewer and smaller convective cores. In summer, increasing core sizes emphasise that convective activity is enhanced over land and sea (Takahashi et al., 2023). Strong organisation occurs in spring (southern hemisphere)and summer (northern hemisphere), especially during the afternoon~~ Interestingly, our findings contrast with Takahashi et al. (2017), as we observe stronger convective organisation - reflected in higher COP and ROME values and lower SCAI values - more frequently over the ocean. Over continental Africa, spatial patches of weak convective organisation appear in both seasons (Section 4.2, Section 4.4.4). However, the difference between land and ocean remain small and may partly stem from an uneven distribution of cloud tracks (Figure 2).

Spatial patterns of convective hotspots show differences over land and ~~at night over the ocean. The diurnal cycle of the organisation indices implies a shift compared to a maximum of convective development (Li et al., 2021). We see a regional peak in organisation over the Atlantic Ocean and coastal West Africa. Organised clouds with larger cores and a prolonged life-cycle appear primarily in the vicinity of the Gulf of Guinea and secondarily in coastal and rainforest regions of~~ ocean. Around the equator, we observe a great share of cloud systems with a weak and strong organisation. This spatial overlap occurs between March–May, in particular over the ocean, and between June–August, especially over continental Africa (Section ~~4.2). Over the tropical Atlantic Ocean, we find lower cloud tops and warmer MCSs, but also high values of ROME and COP. We emphasise that organisation is not only affected by convective intensity (Takahashi et al., 2017). Instead, extra-tropical MCSs may act as additional drivers for convective organisation (Futyan and Genio, 2007). In the southern hemisphere, we find a high variability for convective development and spatio-temporal patterns of organisation. Here, regional circulations and the continental landmass distribution may alter the annual cycle of cloud development, affecting our results (Brune et al., 2020)~~ 4.4.4). Overall, the distribution of convective organisation varies notably between hemispheres and between equatorial and tropical zones (Section 4.3). These differences may be driven by a mix of local surface features (Vondou, 2012), monsoonal dynamics (Futyan and Genio, 2007), and topographic influences such as katabatic flows (Nicholson, 2018). Although our study reveals distinct geographical patterns, isolating the role of topography will require more targeted analysis.

5.3 ~~The role of the ITCZ on large-scale organisation~~

~~We observe a connection between DCCs and spatial patterns of convective organisation following the northward propagation~~ We also detect a link between convective core occurrence and organisation that may follow the northward migration of the ITCZ in ~~summer (Figure 10, 11). The WAM links to the Hadley circulation. As a result, the tropical rain belt over West Africa and the Sahel rainfall are subject to seasonal changes (Jackson et al., 2022). The ITCZ drives the tropospheric circulation(Vondou, 2012). Its seasonal shift affects the microphysical cloud properties through its influence on surface characteristics, solar radiation and~~ boreal summer. As the ~~local circulation (Kniffka et al., 2019). The ITCZ brings greater humidity in the~~ ITCZ shifts, it may alter regional circulation, surface energy balance, and moisture availability — particularly influencing cloud development over the northern Sahel and ~~the Saharain summer. Following, we observe a weaker subtropical subsidencerate over the Sahara and a~~ southern Sahara, as observed by, e.g., the spatial distribution of SCAI between June and August (Section 4.4.3). These changes may be associated with increased humidity, reduced subtropical subsidence, and deeper ascent within the tropical ~~rain belt (Fontaine and Philippon, 2000). The seasonal~~ rainbelt (Fontaine and Philippon, 2000). Together with strengthened meridional pressure gradients ~~strengthen the low-level moisture transport across adjacent regions (Lavaysse et al., 2009)and may lead to the observed promotion of convective activity in the northern hemisphere (Section 4.3). This seasonality is~~ (Lavaysse et al., 2009), they may contribute to the occurrence of large convective systems with multiple cores. This observation may be reflected in our results ~~by an increase of more intense, larger DCCs, larger cloud anvils,~~ as a northward displacement of convective clouds and an increase in cloud area, core area, and core number over continental Africa in July and ~~an enhanced degree of convective organisation between June and~~ August (Section ~~??~~). ~~Although the role of the ITCZ as a prolific producer of rainfall has been studied before, the correlation between organisation and heavy rain requires further investigation (Bao et al., 2024). Analysing an extended time series may offer a more detailed perspective on~~ 4.2, Section 4.3). While our findings highlight the variability of convective organisation, the limited six-month time frame prevents a climatological interpretation. Extending this analysis across multiple years may provide deeper insights into the annual cycle of convective organisation ~~(Takahashi et al., 2017). Furthermore, it may benefit the accuracy and timeliness of operational forecasts~~ and help refine operational forecasting and early-warning systems (Pendergrass, 2020).

~~This study investigates~~

5.3 Uncertainties and limitations

Our analysis may offer additional insights into the spatio-temporal ~~patterns~~ distribution of convective organisation in ~~tropical West Africa using ML-based 3D radar reflectivities. For this purpose, we employ three organisation indices to identify and statistically analyse regional hotspots of convective organisation~~the tropics. However, overall statistical relationships between convective organisation indices and cloud properties remain weak as we observe mostly small to medium effect sizes and low to moderate correlation coefficients (Section 4.2, Section 4.4.2). They highlight the complexity of quantifying convective organisation across space and time. Although our study may help to map patterns of convective organisation across the AOI, gaining a deeper understanding of the underlying processes may require incorporating additional cloud parameters — such as cloud radiative properties - or associated precipitation rates (e.g., Stauffer and Wing (2024); Stubenrauch et al. (2023)). Moreover, addressing the imbalance between land and ocean cloud occurrences could strengthen the robustness of our findings.

Currently, the cloud track distribution is skewed, with a heavy concentration near the equator. ~~Along the AOI, we find the strongest convective organisation in the Atlantic Ocean of the southern hemisphere and the coastal regions of West Africa. The convective activity diverges in regions near the tropics and the equator. Around the equator, we observe concurrent hotspots of~~ Notably, all indices indicate overlapping occurrences of both weak and strong ~~convective organisation in the same region. They superimpose each other, blurring spatial statistics. Overall, the strength of organisation is connected not only to the cluster size and lifetime but also to the number and size of DCCs within a cluster. We detect an increase in convective organisation especially for systems with more than 10 DCCs. While our results agree with previous research, we observe that convective organisation is about 5–10 % stronger over the ocean. However, seasonal and zonal effects account for 10–20 % of~~ organisation within the same regions — particularly over the Atlantic Ocean and continental Africa in spring, and over the Congo River basin in summer. These spatial overlaps may obscure clearer statistical signals (Section 4.4).

Our dataset describes the three-dimensional structure of the ~~organisation index scale. The seasonal analysis of~~ tracked clouds, which may enable segmentation of cloud and core regions across horizontal and vertical dimensions at each point in time. Still, it is constrained by the performance of the ML model and the underlying tracking algorithm. Based on evaluations from Brüning et al. (2024) and Brüning and Tost (2025), the ML-predicted radar reflectivities exhibit a mean error of 2.99 dBZ. While suitable for building contiguous 3D cloud fields, the predictions struggle to accurately represent shallow cumulus and cirrus clouds — limitations inherited from the CloudSat CPR (Sassen and Wang, 2008). Incorporating higher-resolution satellite data or ground-based radar could enhance prediction accuracy. Other sources of uncertainty include the chosen thresholds for the detection algorithm and the ~~percentile locations emphasises a connection between convective clustering and large-scale forcings, such as the shift of the ITCZ. The employed indices show partly ambiguous results. These uncertainties reflect the specific limitations of each index. Current indices cannot sufficiently characterise the degree of convective organisation . Here, ROME shows the highest agreement to previous findings suggesting a a stronger convective organisation over land. Nevertheless, all indices are subject to spatio-temporal variations. Including this variability in an adapted index may benefit the accuracy of the results. In summary, our study emphasises the need to quantify the mechanisms that control convective organisation on a regional level. An in-depth understanding is necessary to improve the representation of convective clouds and enhance a future climate risk assessment.~~ skewed distributions underlying our percentile-based classifications of convective organisation. The indices themselves are sensitive to cloud object count (SCAI) or area (COP, ROME), which may affect spatial patterns, especially since equatorial convective clouds tend to be smaller and more frequent than those near the tropics (Section 2.5, Section 3.1). Additional uncertainties involve the influence of the terrain on cloud organisation (Biagioli and Tompkins, 2023) . Future research could benefit from using combined indices or integrating temporal and spatial factors into a unified metric for 3D data. Our current method uses a moving-window, grid-based approach (Section 3.2), differing from past studies that partitioned the AOI into equal-area subsets (e.g., Tobin et al. (2012); Stubenrauch et al. (2023); Retsch et al. (2020)). While a moving window may reduce noise from small-scale fluctuations, its kernel size is manually chosen. To address this, we plan to explore unsupervised clustering techniques such as DBSCAN or HDBSCAN, which offer more data-driven alternatives. Zuo et al. (2022) successfully applied DBSCAN to identify cloud clusters in 3D radar data, while Kim et al. (2023) used

the approach to derive precipitation probabilities from geostationary satellites. In future work, we aim to test whether such algorithms may reliably quantify convective organisation across space and time.

6 Conclusions

This study explores the spatial and temporal patterns of convective organisation in tropical West Africa using ML-based 3D radar reflectivities. We focus on the relationship between convective organisation, cloud structure, and core properties, using three organisation indices to statistically identify regional hotspots through a percentile-based classification.

7 ~~Impact of the hemisphere on seasonal differences of organised convection~~

~~We complement our findings from Sect. 4.2 and Sect. 4.3 by evaluating whether seasonal differences of organised convection along the hemispheres are statistically significant (Figure ??). The~~ Our analysis reveals that convective organisation tends to be slightly stronger over the ocean. However, differences between the ~~northern (NH) and southern (SH) hemispheres generally agree with the results described in Sect. 4.3. We observe statistically significant differences between the groups regarding the organisation indices and parts of the cloud properties ($p < 0.05$). However, the effect sizes are predominantly small, particularly for the cloud properties (Figure ??, d–i). The results emphasise convective organisation increases in summer (JJA)(Figure ??, a–c). For instance,~~ indices over different surface types and along the period remain low and average around 10–15 %. We observe a considerable spatial variability and a temporal shift in the distribution of strong convective organisation which appears linked to the northward migration of the ITCZ. From March to August, COP and ROME values increase while SCAI decreases, especially in the northern hemisphere, indicating an enhanced spatial clustering of convective clouds. Our regional analysis shows that the most cloud systems with a strong convective organisation during spring (March–May) are concentrated over the Atlantic Ocean and coastal West Africa, predominantly in the southern hemisphere. In summer (June–August), these hotspots shift inland toward the equatorial rainforest, West African Plains, and Sahel region. Notably, both weak and strong convective organisation frequently co-occur in the same regions, complicating statistical interpretation and underscoring the complexity of convective systems.

While correlations between organisation indices and cloud or core properties are generally weak to moderate, we observe that clouds with the 10 % strongest convective organisation tend to have larger cloud areas, lower cloud top and core heights, and more less but larger cores than the average cloud trajectory. In contrast, the 10 % weakest convective organisation are associated with smaller cloud areas, shorter lifetimes, fewer but larger cores, and a lower cloud and core height. Differences in CTH appear to be the most important for identifying cases of strong convective organisation. In contrast, the cloud area, cloud lifetime and number of cores appear to be a driver of weak convective organisation. Despite these findings, observed relationships and spatial patterns vary notably across the indices. The indices themselves often yield opposing results, reflecting their individual sensitivities and limitations. This variability is further influenced by the characteristics of the ~~effect size is higher between the two hemispheres than the seasons (COP, SCAI). Except for the CTH, the distributions of all cloud~~

parameters shift towards a higher mean in NH summer. In the southern hemisphere, the seasonal differences are minor or even reversed. This finding reinforces the assumption of a seasonally opposed pattern for organised convection in the southern and northern hemispheresML-based dataset. As the current study relies on 2D indices, developing a 3D organisation metric could provide a more accurate and holistic view. In summary, our findings highlight substantial variability in convective organisation across time and space. Given its influence on extreme weather, understanding these variations - and the mechanisms behind them - is crucial for improving climate risk assessments and forecasting capabilities in West Africa and beyond.

Boxplot for organised cloud clusters (P90, n = 29 365) grouped by the hemisphere (NH, SH) and season (MAM, JJA). We show **(a)** the COP, **(b)** the SCAI, **(c)** the ROME, **(d)** the cloud anvil area, **(e)** the CTH, **(f)** the cloud lifetime, **(g)** the number of DCCs, **(h)** the convective core area, and **(i)** the area ratio between cloud anvil and core area. The boxplot contains the median (bold black lines) and the arithmetic mean (black diamonds). Annotations depict the effect size measured by Cohen's D and the p-value derived from Welch's t-test (not significant (ns): $p \geq 0.1$, significant with *: $p < 0.1$, **: $p < 0.05$, ***: $p < 0.01$).

Code and data availability. The level 2B-GEOPROF CloudSat data used in this study are available at the CloudSat Data Processing Center at CIRA/Colorado State University and can be retrieved from http://www.CloudSat.cira.colostate.edu/order-data (CloudSat Data Processing Center, 2024). The Meteosat SEVIRI level 1.5 data used in this study is freely and openly available via the EUMETSAT Data Store at https://navigator.eumetsat.int/product/EO-:EUM:DAT:MSG:HRSEVIRI (EUMETSAT Data Services, 2024). The code used in this study will be released upon publication.

Author contributions. S.B and H.T. designed the study. S.B developed the code for performing the analysis and visualisation. S.B. and H.T. contributed to analysing and evaluating spatio-temporal patterns of convective cloud organisation. S.B. and H.T. wrote the draft of the paper. All authors have read and agreed to the published version of the manuscript.

Competing interests. The authors declare that they have no conflict of interest.

Acknowledgements. This work was supported by the project "Big Data in Atmospheric Physics (BINARY)", funded by the Carl Zeiss Foundation (grant P2018-02-003), and the Max Planck Graduate Center with the Johannes Gutenberg University of Mainz (MPGC). We thank EUMETSAT for providing access to the Meteosat SEVIRI imager data and the Cooperative Institute for Research in the Atmosphere, CSU, for providing access to the CloudSat 2B-GEOPROF data.

References

Atiah, W. A., Amekudzi, L. K., and Danuor, S. K.: Mesoscale convective systems and contributions to flood cases in Southern West Africa (SWA): A systematic review, Weather and Climate Extremes, 39, 100 551, https://doi.org/10.1016/j.wace.2023.100551, 2023.

Bao, J., Stevens, B., Kluft, L., and Muller, C.: Intensification of daily tropical precipitation extremes from more organized convection, Sci. Adv., 10, eadj6801, https://doi.org/10.1126/sciadv.adj6801, 2024.

Becker, T., Bechtold, P., and Sandu, I.: Characteristics of convective precipitation over tropical Africa in storm-resolving global simulations, Q. J. R. Meteorol. Soc., 147, 4388–4407, https://doi.org/10.1002/qj.4185, 2021.

Berthou, S., Rowell, D. P., Kendon, E. J., Roberts, M. J., Stratton, R. A., Crook, J. A., and Wilcox, C.: Improved climatological precipitation characteristics over West Africa at convection-permitting scales, Clim. Dyn., 53, 1991–2011, https://doi.org/10.1007/s00382-019-04759-4, 2019.

Biagioli, G. and Tompkins, A. M.: Measuring Convective Organization, Journal of Atmospheric Sciences, 80, 2769–2789, https://doi.org/10.1175/JAS-D-23-0103.1, 2023.

Bläckberg, C. P. O. and Singh, M. S.: Increased Large-Scale Convective Aggregation in CMIP5 Projections: Implications for Tropical Precipitation Extremes, Geophys. Res. Lett., 49, e2021GL097 295, https://doi.org/10.1029/2021GL097295, 2022.

Brune, S., Buschow, S., and Friederichs, P.: Observations and high-resolution simulations of convective precipitation organization over the tropical Atlantic, Q. J. R. Meteorol. Soc., 146, 1545–1563, https://doi.org/10.1002/qj.3751, 2020.

Brüning, S. and Tost, H.: A ML-based perspective on deep convective clouds and their organisation in 3D. Part I: Influence of deep convective cores on the cloud life-cycle, submitted to EGUsphere, 2025.

Brüning, S., Niebler, S., and Tost, H.: Artificial intelligence (AI)-derived 3D cloud tomography from geostationary 2D satellite data, Atmos. Meas. Tech., 17, 961–978, https://doi.org/10.5194/amt-17-961-2024, 2024.

Chen, P.-J., Chen, W.-T., Wu, C.-M., and Yo, T.-S.: Convective Cloud Regimes From a Classification of Object-Based CloudSat Observations Over Asian-Australian Monsoon Areas, Geophys. Res. Lett., 48, e2021GL092 733, https://doi.org/10.1029/2021GL092733, 2021.

CloudSat Data Processing Center: Data Products, CloudSat DPC [data set], https://www.cloudsat.cira.colostate.edu/data-products, accessed: 2024-12-12, 2024.

Cohen, J.: Statistical Power Analysis for the Behavioral Sciences, Routledge, 2 edn., https://doi.org/10.4324/9780203771587, 2013.

Coppin, D. and Bony, S.: Physical mechanisms controlling the initiation of convective self-aggregation in a General Circulation Model, J. Adv. Model. Earth Syst., 7, 2060–2078, https://doi.org/10.1002/2015MS000571, 2015.

Cui, W., Dong, X., Xi, B., and Feng, Z.: Climatology of Linear Mesoscale Convective System Morphology in the United States Based on the Random-Forests Method, J. Clim., 34, 7257–7276, https://doi.org/10.1175/JCLI-D-20-0862.1, 2021.

Dauhut, T., Chaboureau, J.-P., Escobar, J., and Mascart, P.: Giga-LES of Hector the Convector and Its Two Tallest Updrafts up to the Stratosphere, Journal of Atmospheric Sciences, 73, 5041–5060, https://doi.org/10.1175/JAS-D-16-0083.1, 2016.

Derrick, B. and White, P.: Why Welch's test is Type I error robust, TQMP, 12, 30–38, https://doi.org/10.20982/tqmp.12.1.p030, 2016.

Esmaili, R. B., Tian, Y., Vila, D. A., and Kim, K.-M.: A Lagrangian analysis of cold cloud clusters and their life cycles with satellite observations, J. Geophys. Res. Atmos., 121, 11,723–11,738, https://doi.org/10.1002/2016JD025653, 2016.

EUMETSAT Data Services: High Rate SEVIRI Level 1.5 Image Data - MSG - 0 degree, https://navigator.eumetsat.int/product/EO:EUM:DAT:MSG:HRSEVIRI, accessed: 2024-12-12, 2024.

Feng, Z., Varble, A., Hardin, J., Marquis, J., Hunzinger, A., Zhang, Z., and Thieman, M.: Deep Convection Initiation, Growth, and Environments in the Complex Terrain of Central Argentina during CACTI, Mon. Weather Rev., 150, 1135–1155, https://doi.org/10.1175/MWR-D-21-0237.1, 2022.

Fink, A. H., Vincent, D. G., and Ermert, V.: Rainfall Types in the West African Sudanian Zone during the Summer Monsoon 2002, Mon. Weather Rev., 134, 2143–2164, https://doi.org/10.1175/MWR3182.1, 2006.

Fontaine, B. and Philippon, N.: Seasonal evolution of boundary layer heat content in the West African monsoon from the NCEP/NCAR reanalysis (1968–1998), Int. J. Climatol., 20, 1777–1790, https://doi.org/10.1002/1097-0088(20001130)20:14<1777::AID-JOC568>3.0.CO;2-S, 2000.

Futyan, J. M. and Genio, A. D. D.: Deep Convective System Evolution over Africa and the Tropical Atlantic, J. Clim., 20, 5041–5060, https://doi.org/10.1175/JCLI4297.1, 2007.

Haerter, J. O., Böing, S. J., Henneberg, O., and Nissen, S. B.: Circling in on Convective Organization, Geophys. Res. Lett., 46, 7024–7034, https://doi.org/10.1029/2019GL082092, 2019.

Hartmann, D. L., Hendon, H. H., and Houze, R. A.: Some Implications of the Mesoscale Circulations in Tropical Cloud Clusters for Large-Scale Dynamics and Climate, Journal of Atmospheric Sciences, 41, 113–121, https://doi.org/10.1175/1520-0469(1984)041<0113:SIOTMC>2.0.CO;2, 1984.

Heikenfeld, M., Marinescu, P. J., Christensen, M., Watson-Parris, D., Senf, F., van den Heever, S. C., and Stier, P.: tobac 1.2: towards a flexible framework for tracking and analysis of clouds in diverse datasets, Geosci. Model Dev., 12, 4551–4570, https://doi.org/10.5194/gmd-12-4551-2019, 2019.

Held, I. M., Hemler, R. S., and Ramaswamy, V.: Radiative-Convective Equilibrium with Explicit Two-Dimensional Moist Convection, Journal of Atmospheric Sciences, 50, 3909–3927, https://doi.org/10.1175/1520-0469(1993)050<3909:RCEWET>2.0.CO;2, 1993.

Houze, R. A.: Structure and Dynamics of a Tropical Squall–Line System, Mon. Wea. Rev., 105, 1540–1567, https://doi.org/10.1175/1520-0493(1977)105<1540:SADOAT>2.0.CO;2, 1977.

Igel, M. R., Drager, A. J., and van den Heever, S. C.: A CloudSat Cloud-Object Partitioning Technique and Assessment and Integration of Deep Convective Anvil Sensitivities to Sea Surface Temperature, J. Geophys. Res. Atmos., 119, 10 515–10 535, https://doi.org/10.1002/2014JD021717, 2014.

Jackson, L. S., Marsham, J. H., Parker, D. J., Finney, D. L., Fitzpatrick, R. G. J., Rowell, D. P., Stratton, R. A., and Tucker, S.: The Effect of Explicit Convection on Climate Change in the West African Monsoon and Central West African Sahel Rainfall, J. Clim., 35, 1537–1557, https://doi.org/10.1175/JCLI-D-21-0258.1, 2022.

Jin, D., Oreopoulos, L., Lee, D., Tan, J., and Kim, K.-m.: A New Organization Metric for Synoptic Scale Tropical Convective Aggregation, J. Geophys. Res. Atmos., 127, e2022JD036 665, https://doi.org/10.1029/2022JD036665, 2022.

Jones, W., Christensen, M., and Stier, P.: A semi-Lagrangian method for detecting and tracking deep convective clouds in geostationary satellite observations, Atmos. Meas. Tech., 16, 1043–1059, https://doi.org/10.5194/amt-16-1043-2023, 2023.

Jones, W., Stengel, M., and Stier, P.: A Lagrangian perspective on the lifecycle and cloud radiative effect of deep convective clouds over Africa, Atmos. Chem. Phys., 24, 5165–5180, https://doi.org/10.5194/acp-24-5165-2024, 2024.

Kim, D., Kim, H.-J., and Choi, Y.-S.: Unsupervised Clustering of Geostationary Satellite Cloud Properties for Estimating Precipitation Probabilities of Tropical Convective Clouds, J. Appl. Meteorol., 62, 1083–1094, https://doi.org/10.1175/JAMC-D-22-0175.1, 2023.

Klein, C., Nkrumah, F., Taylor, C. M., and Adefisan, E. A.: Seasonality and Trends of Drivers of Mesoscale Convective Systems in Southern West Africa, J. Clim., 34, 71–87, https://doi.org/10.1175/JCLI-D-20-0194.1, 2021.

Kniffka, A., Knippertz, P., and Fink, A. H.: The role of low-level clouds in the West African monsoon system, Atmos. Chem. Phys., 19, 1623–1647, https://doi.org/10.5194/acp-19-1623-2019, 2019.

Lavaysse, C., Flamant, C., Janicot, S., Parker, D. J., Lafore, J.-P., Sultan, B., and Pelon, J.: Seasonal evolution of the West African heat low: a climatological perspective, Clim. Dyn., 33, 313–330, https://doi.org/10.1007/s00382-009-0553-4, 2009.

Li, W., Zhang, F., Yu, Y., Iwabuchi, H., Shen, Z., Wang, G., and Zhang, Y.: The semi-diurnal cycle of deep convective systems over Eastern China and its surrounding seas in summer based on an automatic tracking algorithm, Clim. Dyn., 56, 357–379, https://doi.org/10.1007/s00382-020-05474-1, 2021.

Luo, Z., Liu, G. Y., and Stephens, G. L.: CloudSat adding new insight into tropical penetrating convection, Geophys. Res. Lett., 35, L19 819, https://doi.org/10.1029/2008GL035330, 2008.

Mandorli, G. and Stubenrauch, C. J.: Assessment of object-based indices to identify convective organization, Geosci. Model Dev., 17, 7795–7813, https://doi.org/10.5194/gmd-17-7795-2024, 2024.

Mapes, B. and Neale, R.: Parameterizing Convective Organization to Escape the Entrainment Dilemma, J. Adv. Model. Earth Syst., 3, M06 004, https://doi.org/10.1029/2011MS000042, 2011.

Marchand, R., Mace, G. G., Ackerman, T., and Stephens, G.: Hydrometeor Detection Using Cloudsat—An Earth-Orbiting 94-GHz Cloud Radar, J. Atmos. Oceanic Tech., 25, 519–533, https://doi.org/10.1175/2007JTECHA1006.1, 2008.

Muller, C. and Bony, S.: What favors convective aggregation and why?, Geophys. Res. Lett., 42, 5626–5634, https://doi.org/10.1002/2015GL064260, 2015.

Nicholson, S. E.: The ITCZ and the Seasonal Cycle over Equatorial Africa, BAMS, 99, 337–348, https://doi.org/10.1175/BAMS-D-16-0287.1, 2018.

Pendergrass, A. G.: Changing Degree of Convective Organization as a Mechanism for Dynamic Changes in Extreme Precipitation, Curr. Clim. Change Rep., 6, 47–54, https://doi.org/10.1007/s40641-020-00157-9, 2020.

Prein, A. F., Feng, Z., Fiolleau, T., Moon, Z. L., Núñez Ocasio, K. M., Kukulies, J., Roca, R., Varble, A. C., Rehbein, A., Liu, C., Ikeda, K., Mu, Y., and Rasmussen, R. M.: Km-Scale Simulations of Mesoscale Convective Systems Over South America—A Feature Tracker Intercomparison, J. Geophys. Res. Atmos., 129, e2023JD040 254, https://doi.org/10.1029/2023JD040254, 2024.

Pscheidt, I., Senf, F., Heinze, R., Deneke, H., Trömel, S., and Hohenegger, C.: How organized is deep convection over Germany?, Q. J. R. Meteorol. Soc., 145, 2366–2384, https://doi.org/10.1002/qj.3552, 2019.

Rempel, M., Senf, F., and Deneke, H.: Object-Based Metrics for Forecast Verification of Convective Development with Geostationary Satellite Data, Mon. Wea. Rev., 145, 3161–3178, https://doi.org/10.1175/MWR-D-16-0480.1, 2017.

Retsch, M. H., Jakob, C., and Singh, M. S.: Assessing Convective Organization in Tropical Radar Observations, J. Geophys. Res. Atmos., 125, e2019JD031 801, https://doi.org/10.1029/2019JD031801, 2020.

Ronneberger, O., Fischer, P., and Brox, T.: U-Net: Convolutional Networks for Biomedical Image Segmentation, in: Medical Image Computing and Computer-Assisted Intervention – MICCAI 2015, edited by Navab, N., Hornegger, J., Wells, W. M., and Frangi, A. F., vol. 9351, pp. 234–241, Springer International Publishing, Cham, 2015.

Sassen, K. and Wang, Z.: Classifying clouds around the globe with the CloudSat radar: 1-year of results, Geophys. Res. Lett., 35, L04 805, https://doi.org/10.1029/2007GL032591, 2008.

Schmetz, J., Pili, P., Tjemkes, S., Just, D., Kerkmann, J., Rota, S., and Ratier, A.: An introduction to Metetsat second generation (MSG), BAMS, 83, 977–992, https://doi.org/10.1175/1520-0477(2002)083<0977:AITMSG>2.3.CO;2, 2002.

Semie, A. G. and Bony, S.: Relationship Between Precipitation Extremes and Convective Organization Inferred From Satellite Observations, Geophys. Res. Lett., 47, e2019GL086 927, https://doi.org/10.1029/2019GL086927, 2020.

Sokolowsky, G. A., Freeman, S. W., Jones, W. K., Kukulies, J., Senf, F., Marinescu, P. J., Heikenfeld, M., Brunner, K. N., Bruning, E. C., Collis, S. M., Jackson, R. C., Leung, G. R., Pfeifer, N., Raut, B. A., Saleeby, S. M., Stier, P., and van den Heever, S. C.: *tobac* v1.5: introducing fast 3D tracking, splits and mergers, and other enhancements for identifying and analysing meteorological phenomena, Geosci. Model Dev., 17, 5309–5330, https://doi.org/10.5194/gmd-17-5309-2024, 2024.

Stauffer, C. L. and Wing, A. A.: How Does Organized Convection Impact Explicitly Resolved Cloud Feedbacks in the Radiative-Convective Equilibrium Model Intercomparison Project?, Journal of Advances in Modeling Earth Systems, 16, e2023MS003 924, https://doi.org/https://doi.org/10.1029/2023MS003924, 2024.

Stephens, G. L., Vane, D. G., Tanelli, S., Im, E., Durden, S., Rokey, M., Reinke, D., Partain, P., Mace, G. G., Austin, R., L'Ecuyer, T., Haynes, J., Lebsock, M., Suzuki, K., Waliser, D., Wu, D., Kay, J., Gettelman, A., Wang, Z., and Marchand, R.: CloudSat mission: Performance and early science after the first year of operation, J. Geophys. Res. Atmos., 113, https://doi.org/10.1029/2008JD009982, 2008.

Stubenrauch, C. J., Mandorli, G., and Lemaitre, E.: Convective organization and 3D structure of tropical cloud systems deduced from synergistic A-Train observations and machine learning, Atmos. Chem. Phys., 23, 5867–5884, https://doi.org/10.5194/acp-23-5867-2023, 2023.

Takahashi, H., Luo, Z. J., and Stephens, G. L.: Level of neutral buoyancy, deep convective outflow, and convective core: New perspectives based on 5 years of CloudSat data, J. Geophys. Res. Atmos., 122, 2958–2969, https://doi.org/10.1002/2016JD025969, 2017.

Takahashi, H., Luo, Z. J., Stephens, G., and Mulholland, J. P.: Revisiting the Land-Ocean Contrasts in Deep Convective Cloud Intensity Using Global Satellite Observations, Geophys. Res. Lett., 50, e2022GL102 089, https://doi.org/10.1029/2022GL102089, 2023.

Tan, J., Jakob, C., Rossow, W. B., and Tselioudis, G.: Increases in tropical rainfall driven by changes in frequency of organized deep convection, Nature, 519, 451–454, https://doi.org/10.1038/nature14339, 2015.

Taylor, C. M., Klein, C., Dione, C., Parker, D. J., Marsham, J., Diop, C. A., Fletcher, J., Chaibou, A. A. S., Nafissa, D. B., Semeena, V. S., Cole, S. J., and Anderson, S. R.: Nowcasting tracks of severe convective storms in West Africa from observations of land surface state, Environ. Res. Lett., 17, 034 016, https://doi.org/10.1088/1748-9326/ac536d, 2022.

Tobin, I., Bony, S., and Roca, R.: Observational Evidence for Relationships between the Degree of Aggregation of Deep Convection, Water Vapor, Surface Fluxes, and Radiation, J. Clim., 25, 6885–6904, https://doi.org/10.1175/JCLI-D-11-00258.1, 2012.

Tompkins, A. M. and Semie, A. G.: Organization of tropical convection in low vertical wind shears: Role of updraft entrainment, J. Adv. Model. Earth Syst., 9, 1046–1068, https://doi.org/10.1002/2016MS000802, 2017.

Vondou, D. A.: Spatio-Temporal Variability of Western Central African Convection from Infrared Observations, Atmos., 3, 377–399, https://doi.org/10.3390/atmos3030377, 2012.

White, B. A., Buchanan, A. M., Birch, C. E., Stier, P., and Pearson, K. J.: Quantifying the Effects of Horizontal Grid Length and Parameterized Convection on the Degree of Convective Organization Using a Metric of the Potential for Convective Interaction, Journal of Atmospheric Sciences, 75, 425–450, https://doi.org/10.1175/JAS-D-16-0307.1, 2018.

Wing, A. A. and Emanuel, K. A.: Physical mechanisms controlling self-aggregation of convection in idealized numerical modeling simulations, JAMES, 6, 59–74, https://doi.org/10.1002/2013MS000269, 2014.

Wing, A. A., Emanuel, K., Holloway, C. E., and Muller, C.: Convective Self-Aggregation in Numerical Simulations: A Review, Surv. Geophys., 38, 1173–1197, https://doi.org/10.1007/s10712-017-9408-4, 2017.

Wing, A. A., Stauffer, C. L., Becker, T., Reed, K. A., Ahn, M.-S., Arnold, N. P., Bony, S., Branson, M., Bryan, G. H., Chaboureau, J.-P., De Roode, S. R., Gayatri, K., Hohenegger, C., Hu, I.-K., Jansson, F., Jones, T. R., Khairoutdinov, M., Kim, D., Martin, Z. K., Matsugishi, S., Medeiros, B., Miura, H., Moon, Y., Müller, S. K., Ohno, T., Popp, M., Prabhakaran, T., Randall, D., Rios-Berrios, R., Rochetin, N., Roehrig, R., Romps, D. M., Ruppert Jr., J. H., Satoh, M., Silvers, L. G., Singh, M. S., Stevens, B., Tomassini, L., van Heerwaarden, C. C., Wang, S., and Zhao, M.: Clouds and Convective Self-Aggregation in a Multimodel Ensemble of Radiative-Convective Equilibrium Simulations, Journal of Advances in Modeling Earth Systems, 12, e2020MS002 138, https://doi.org/https://doi.org/10.1029/2020MS002138, 2020.

Zipser, E. J., Cecil, D. J., Liu, C., Nesbitt, S. W., and Yorty, D. P.: Where are the most intense thunderstorms on earth?, BAMS, 87, 1057–1072, https://doi.org/10.1175/BAMS-87-8-1057, 2006.

Zuo, Y., Hu, Z., Yuan, S., Zheng, J., Yin, X., and Li, B.: Identification of Convective and Stratiform Clouds Based on the Improved DBSCAN Clustering Algorithm, Adv. Atmos. Sci., 39, 2203–2212, https://doi.org/10.1007/s00376-021-1223-7, 2022.